PREDICTION AND CONTROL OF PATTERNED ACTIVITY IN SMALL NEURAL NETWORKS

A Dissertation
Presented to
The Academic Faculty

by

Fred H. Sieling

In Partial Fulfillment
of the Requirements for the Degree
Doctor of Philosophy in the
School of Biomedical Engineering

Georgia Institute of Technology
December 2010

PREDICTION AND CONTROL OF PATTERNED ACTIVITY IN SMALL NEURAL NETWORKS

Approved by:

Dr. Astrid A. Prinz, Advisor
Department of Biology
Emory University

Dr. Ronald L. Calabrese
Department of Biology
Emory University

Dr. Robert J. Butera, co-Advisor
School of Biomedical Engineering
Georgia Institute of Technology

Dr. Stephen P. DeWeerth
School of Biomedical Engineering
Georgia Institute of Technology

Dr. Carmen C. Canavier
Department of Ophthalmology
Louisiana State University

Date Approved: July 23, 2010

ACKNOWLEDGEMENTS

First, thank you to the big intellectual contributors to this work. Astrid, Carmen, and Rob, thanks so much for your time. You made yourselves available for all sorts of questions, prepositions, and suppositions. I'd like to know how you managed that while at the same time balancing everything else that you are each responsible for.

Now to France. Romuald and John, you made the last third of my PhD fun and exciting. Thanks for being open-minded and welcoming me to your lab in Bordeaux.

To my committee, thank you for your time. At our meetings, you listened and gave me the guidance I needed.

To a lot of other people… The Prinz lab: Tomasz for kafchi service, Andrei and Cengiz for tons of puns, Ryan for the right foot. Santiago and Amber for music and for cleaning the tanks. Other professionals: Selva and Patrick for years of chats. To Jeremy, Dieter, Nathan, Eric, and the whole foosball crew- thanks for letting me win.

Family, friends, others... My folks. You know what you did. Thanks guys!

TABLE OF CONTENTS

LIST OF TABLES

LIST OF FIGURES

SUMMARY

Rhythmic neural activity is thought to underlie many high-level functions of the nervous system. Our goals are to understand rhythmic activity starting with small networks, using theoretical and experimental tools. Phase resetting theory describes essential properties that cause and destroy rhythms. We validate and extend one branch of this theory, testing it in bursting neurons coupled by excitation and then extending the theory to account for temporal variability found in our experimental data. We show that the theory makes good predictions of rhythmic activity in heterogeneous networks. We also note differences in mathematical structure between inhibition- and excitation-coupling that cause them to behave differently in noisy contexts and may explain why all central pattern generators (CPGs) found in nature are dominated by inhibition. Our extension of the theory gives a method that is useful to compare experimental and model data and shows that noise may either create or destroy a rhythm. Finally, we described the cellular mechanisms in *Aplysia* that switch the feeding CPG from arrhythmic to rhythmic behavior in response to reward stimuli. Previous studies showed that a Dopamine reward signal is correlated to changes in electrical coupling and excitability in several important neurons in the CPG. Using the dynamic clamp and an *in vitro* analog of the full behavioral system, we were able to determine that electrical coupling alone controls rhythmicity, while excitability independently controls the rate of activity. These results beg for further study, including new theory to explain them fully.

CHAPTER 1: INTRODUCTION

Introduction

The central problem in neuroscience is "how does the brain work." Particularly, what is experience, cognition, memory, consciousness, etc.? Answers to this question have implications in biology, physics, mathematics, and the engineering of information processing and storage systems. Since Ramon y Cajal drew them for us to see, our best answer has been that complex networks of neurons are responsible for brain function.
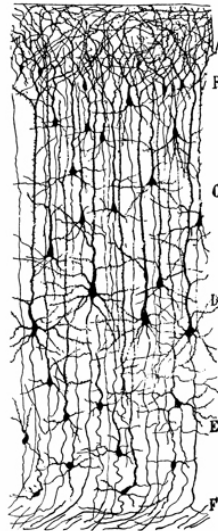
This drawing by Santiago Ramon y Cajal first appeared in volume two, part two of Cajal's Textura del Sistema Nervioso del Hombre y de los Vertebrados, published in Madrid in 1904. The image shows the six layers of the mouse neocortex, labeled A through F, in Cajal's hand. Cajal's drawings provided the foundation of modern neuroanatomy by showing that the nervous system is composed of individual nerve cells, as opposed to a web of continuous elements. (caption is quoted from www.sfn.org)

Information processing and storage in the human brain is well studied, yet it is impossible to say that we understand it. Network structure, rate coding, and temporal coding are some of the major mechanisms that have been discovered to contain information (Dayan and Abbott 2001). The work presented here includes predictions of

temporal coding in chapters 2 and 3 and manipulations of network structure in Chapter 4. Network structure contains information in the specification of connectivity- which spikes are routed to where and how strong is their effect. Rate coding contains information as a rate of spiking. Temporal coding describes information contained by the exact timing of spikes.

As titled, this thesis is about prediction and control. We aimed to generate and verify general scalable phenomenological methods to predict complex neural network activity based on measures from isolated component neurons. Our goal was to find rules connecting properties of isolated component neurons—activity, coupling type, coupling strength, variability, mode switching (bistability), stability—to network behaviors— activity, phase-locking, variability, bistability, stability. Then we aimed to analyze specific mechanistic methods of control to understand high-value biological pattern generation, with emphasis on the biological relevance of studied networks. The following chapters contain more detailed introduction sections relevant to their subject matter.

Specific aims

Aim 1- How well do pulsatile coupling methods work for predicting activity of excitatory networks of 2 bursting neural oscillators?

We generated phase response curves (PRCs) by measuring phase-shifting effects of a synaptic input due to a presynaptic burst on the current cycle (first order PRC) as well as the subsequent cycle (second order PRC) in periodically bursting model and experimental neurons in the pyloric network of the stomatogastric ganglion (STG) of the lobster *Homarus americanus*. A heterogeneous mix of synapse strengths, intrinsic

frequencies, and duty cycles were used to construct hybrid networks consisting of one experimental and one model neuron. Network observations were compared to predictions made from PRCs of component neurons to determine whether 1:1 modes can be successfully predicted in networks coupled by excitation and to show how biological variability (or noise) affects these predictions.

Aim 2- Can we change our prediction methods to accurately incorporate the effects of biological variability in networks of two neurons?

A firing time map was constructed based on the PRCs of each component neuron and used to iterate through the firing of each neuron until N=M bursts had been observed, where M is the number of bursts observed experimentally. The novelty aspect of this work is that we included phase-dependent noise in the PRC, as PRCs are measured experimentally. Using circular statistics, results from the firing time map are compared to experimental observations and predictions from the noiseless method used in aim 1.

Aim 3- Using the dynamic clamp, can we reproduce the effects of a behavioral training paradigm?

We described the cellular mechanisms in *Aplysia* that switch the feeding CPG from arrhythmic to rhythmic behavior in response to reward stimuli. Previous studies showed that a Dopamine reward signal is correlated to changes in electrical coupling and excitability in several important neurons in the CPG. Using the dynamic clamp and an *in vitro* analog of the full behavioral system, we were able to determine that electrical coupling alone causes rhythmicity, while excitability independently controls the rate of activity.

Lay introduction

The central problem in neuroscience is "how does the brain work?" Particularly-what is experience, cognition, memory, conscience, etc.? Answers to this question have potentially huge implications in the engineering of information processing and storage systems and influence a large part of modern physics. Since Ramon y Cajal drew them for us to see, our best answer has been that complex networks of neurons are responsible for brain function. The physical complexity of this cell type—still but one of many in the brain—is staggering, with humans averaging 20 billion neurons per brain, ~100 described types of neurons in the literature, each neuron connecting to many other neurons in type- or function-dependent graphs, and yet untold dynamic variations. All these cells interact incessantly, roughly robustly, and all while their internal working parts are being used, adjusted, destroyed, and replaced. That is the situation under non-pathological conditions.

Neurons communicate electrically. They have wonderful electrically insulated membranes that maintain and conduct electrical signals, supported by a rich cast of voltage-sensitive membrane-bound proteins. In the era of modern computing, this is a benefit to us because we can easily record electrical signals coming from a neuron or likewise stimulate them.

Given that something interesting is going on in and between neurons, we choose to study neurons that are accessible and identifiable. Accessibility allows greater experimental flexibility. These tend to be motor neurons that reach out away from other neurons to innervate muscle tissue, where we can measure and stimulate them easily using a wire placed nearby. Alternatively, any neurons that are located in peripheral ganglia with a few other neurons are relatively easy to find and work with. Identification

allows for an increased measure of explicitly repeatable experiments. In this case, we can know what set of voltage-dependent membrane and intracellular processes is present, which other neurons this one connects to, whether those connections are chemical or electrical, if chemical- what transmitting and receiving molecules are used, how this relationship depends on environmental or behavioral context, and sometimes what significance the neuron plays in transmitting its signal. In an animal with ~20,000 neurons like a lobster or *Aplysia* (sea hare), several functional groups of neurons have been identified. In the human brain, with 20 billion neurons, few have, and progress is… sluggish.

Are all neurons created equal? Why do you study sea animals if you're interested in the human brain? Much of what we now know about the human brain stems from the work in giant squid, lamprey, snails, and lobsters. For example, first descriptions of voltage-dependence of ion channels, central pattern generators, neurotransmitters, neuromodulators, adaptation, synaptic scaling, and conditioned responses. In general, the basic knowledge about how neurons work comes from basic systems, those that are amenable to strong experimental manipulation.

Now that I've laid out my motivation and hopefully answered some of your initial questions, this is what I did. Of course I couldn't have done any of this alone (see *Acknowledgements*). My goal was to develop and test methods to capture the functional essence of neural networks as they exist in biology. The testing process implicitly requires knowledge of the biology, so basic research was also important. In the order presented, I 1) tested some methods, 2) extended those methods, and 3) did basic research

into how neural networks learn, which may result in new or improved methods at a future date.

CHAPTER 2: PREDICTIONS OF PHASE-LOCKING IN EXCITATORY HYBRID NETWORKS: EXCITATION DOES NOT PROMOTE PHASE-LOCKING IN PATTERN-GENERATING NETWORKS AS RELIABLY AS INHIBITION

The majority of this chapter was published in 2009 (Sieling et al. 2009). The PRC morphology section is part of another paper (Maran et al. 2010).

Introduction

Synchrony, or phase-locked activity, is thought to underlie complex biological phenomena such as memory, facial recognition, circadian rhythms, and epileptic seizures (Rodriguez et al. 1999; Fell et al. 2001; de la Iglesia et al. 2004). These phenomena are thought to be emergent in the sense that they arise from self-organization of the component elements and cannot be predicted from the individual components without considering their interactions (Strogatz 2003). The most accessible preparations in which to study these phenomena are central pattern generating networks (CPGs). A CPG is a neural network that generates rhythmic output in the absence of rhythmic input. Here we address two outstanding problems in the field: to develop a framework for understanding how patterns emerge from CPGs, and to gain insight into the preponderance of inhibitory synapses in such networks.

In order to gain insight into CPGs, we chose to start with the simplest possible hybrid network comprised of one bursting neuron and one model neuron. Hybrid network construction has the advantage of providing a controlled environment for testing our

7

methodology that incorporates an actual biological neuron and realistic synapses. Endogenously bursting neurons have been shown to be important in the pyloric network (Hartline 1979; Hartline and Gassie 1979; Miller and Selverston 1982), the heartbeat of crustaceans (Tazaki and Cooke 1990), the gastric CPGs of the crustacean stomatogastric system (Selverston and Moulins 1987; Harris-Warrick et al. 1992; Panchin et al. 1993), the feeding CPG in mollusks (Arshavsky et al. 1989; Arshavsky et al. 1991), and appetitive conditioning in the buccal ganglia of *Aplysia* (Nargeot et al. 1997; Nargeot et al. 2007). Therefore we chose to examine circuits constructed with endogenous bursters. For the biological neuron, we chose the pacemaking kernel of the pyloric network of the stomatogastric ganglion (STG) in *Homarus americanus* (Fig. 1A), comprised of three neurons, the anterior burster (AB) neuron and two pyloric dilator (PD) neurons. The AB/PD complex is electrically coupled, and we consider it to be a single functional unit, which we henceforth refer to as the biological neuron. The biological neuron was isolated pharmacologically and coupled to a bursting model neuron via excitatory synapses using the dynamic clamp (Fig. 1B).

Figure 1. Experimental setup. A: Simplified pyloric network. The pacemaking kernel (AB/PD complex) consists of the AB and PD neurons, which are coupled via gap junctions. B: Schematic of the dynamic clamp. The membrane voltage recorded in the AB/PD complex was used to calculate synaptic current (I_{syn}) received by the model cell. The model cell was updated in real time, and the updated model neuron's membrane voltage was used to calculate I_{syn} received by the AB/PD complex. C: Measurement of phase resetting in a biological neuron. Shown is a membrane potential recording from a free-running AB/PD complex with intrinsic period P_0, perturbed at *ts* (dotted vertical line) by a an excitatory synaptic input, g_{syn}=60nS and *duration*=650ms. An upward crossing of the voltage threshold (horizontal dashed line, see *Phase response curves*) was defined as the start of a burst and assigned a phase of zero. The first burst after the perturbation was advanced such that the first perturbed period P_1 was less than P_0. The subsequent period P_2 was delayed by a small amount such that $P_2>P_0$. In this case, a new burst was triggered after a short delay of 100ms, so that $P_1>ts$ and *tr*=100ms. D: Measurement of phase resetting in a model neuron. Analogous to the biological neuron, the free-running model neuron was perturbed at *ts* by an excitatory synaptic input with g_{syn}=60nS. This perturbation was strong and triggered a new burst immediately, such that $P_1\approx ts$ and *tr*≈0. The burst threshold is shown as a horizontal dashed line. (Panel B adapted from DailyClipArt.net.)

A phase response curve (PRC) tabulates the effect of a perturbation on cycle length as a function of the phase at which it is delivered. Our methods use the PRCs of individual component neurons measured in the open loop configuration with unidirectional synaptic stimuli (Fig. 1C, D) to predict patterned activity in the closed loop

network configuration with bidirectional coupling. Several assumptions are required so that these PRCs can be used to predict the activity of a network. First, we assume that all component neurons in our circuits exhibit an oscillation in the membrane potential that drives bursting. Quiescent or tonically spiking neurons in the circuit are not within the scope of our methods. Second, we assume that the input received in the closed network is similar to that used to generate the PRC. We do not require the weak coupling assumption that is often used in network analysis (Ermentrout and Chow 2002; Netoff et al. 2005; Mancilla et al. 2007) and that assumes phase response is linear. Instead, we make a third assumption, that the effects of one input die out before the next one is received. This approach treats the perturbation as a whole, reducing the analysis to a cycle-by-cycle mapping, and is equally valid for weak or strong coupling. We consider only 1:1 phase-locking between two bursting neurons in which a stable pattern of activity is established in which each neuron fires one burst per cycle.

These methods have to date been evaluated in model networks (Canavier et al. 1997; Canavier et al. 1999; Luo et al. 2004; Achuthan and Canavier 2008; Gurel Kazanci et al. 2008; Maran and Canavier 2008; Oh and Matveev 2008) as well as in hybrid networks coupled with inhibition (Oprisan et al. 2004). Here we test the applicability of PRC-based firing time maps (Ermentrout and Chow 2002) to excitatory coupling of significant strength and duration, using a wide range of synaptic strengths (from 1nS to 10,000nS) and input durations (from 0.3 to 1.5s).

Our motivation for studying excitatory synapses was in part to understand why they are less commonly observed in CPGs, as all known real CPGs are dominated by inhibitory synapses. Leech heartbeat (Calabrese and Peterson 1983), stomatogastric

ganglion (Marder and Calabrese 1996), lamprey swimming (Cangiano and Grillner 2005), salamander locomotor (Cheng et al. 1998), and mammalian locomotor (McCrea and Rybak 2008) CPGs are all functionally dominated by inhibitory synapses, as evidenced by the lack of a single identified excitatory synapse in the first two systems listed. We present experimental and theoretical data showing that a CPG dominated by typical excitatory synapses would need to be carefully tuned to function and in many configurations would be highly sensitive to noise.

Methods

Electrophysiology

Homarus americanus were purchased from Inland Seafood (Atlanta, GA). They were maintained in artificial seawater at 10–14ºC until used. The stomatogastric nervous system was dissected and pinned out in a dish coated with Sylgard (Dow Corning, Midland, MI), and the STG was desheathed with fine forceps. Throughout the experiments, the stomatogastric nervous system was superfused with chilled (9–14ºC) saline containing (in mM) NaCl, 479; KCl, 12; $CaCl_2$, 18; $MgSO_4$, 20; Na_2SO_4, 4; HEPES, 5; pH 7.45. Extracellular recordings were made with stainless steel pin electrodes in Vaseline wells on the motor nerves and amplified with a differential AC amplifier (Model 1700, A-M Systems, Carlsborg, WA). Intracellular recordings from cells in the STG were obtained with an Axoclamp-2B amplifier (Axon Instruments, Foster City, CA) in discontinuous current clamp (DCC) mode using microelectrodes filled with 0.6M K_2SO_4 and 20mM KCl; electrode resistances were in the range of 10–25MΩ. Extracellular and intracellular voltage traces were digitized with a Digidata

1200A board (Axon Instruments), recorded using Clampex 9.2 software (Axon Instruments), and analyzed with Spike2 (Cambridge Electronic Design), Matlab (The MathWorks), and in-house software. The AB and PD neurons were identified based on their membrane potential waveforms, the timing of their activity in the pyloric rhythm, and, for PD only, their axonal projections to the appropriate motor nerves. The only chemical synaptic feedback to the pyloric pacemaker group through the lateral pyloric neuron (LP) to PD inhibitory synapse was removed by applying 0.01mM picrotoxin to the bath. The pharmacologically isolated pyloric pacemaker was monitored by impaling either the AB neuron or one of the PD neurons (Fig 1A). Experimental preparations were discarded when the pacemaking kernel did not burst consistently.

Dynamic clamp

We recorded the membrane potential of the AB/PD complex and used the dynamic clamp (Sharp et al. 1993; Sharp et al. 1993; Prinz et al. 2004) to measure biological PRCs and to construct hybrid networks consisting of the AB/PD complex and a model neuron coupled by artificial synapses (Fig. 1B). The membrane potential at the AB or PD cell body was amplified, fed into a National Instruments DAQ board (PCI-6051E) and digitized at 20kHz. Dynamic clamp programs were written in C^{++} and designed to use the Real Time Linux Dynamic Controller (RTLDC) (Dorval et al. 2001). One program was written to measure the biological PRC. This program used a membrane potential threshold to detect bursts in the ongoing AB or PD rhythm and monitored the cycle period. Artificial synaptic stimuli were injected at different phases of the rhythm by playing a saved synaptic activation waveform into the artificial synapse

(see *Phase response curves*). This stimulus was a conductance waveform used to calculate the momentary current that would flow through the cell membrane at a given time if the stimulus conductance were present in the membrane. To inject this momentary synaptic current into the AB or PD neuron, the program computed the corresponding command voltage, which was turned into an analog voltage by the DAQ board and sent to the electrode amplifier in order to compute the synaptic current described in the next section using the command voltage as $V_{post.}$.

A second program was written to construct hybrid networks. This program implemented two artificial synapses to couple the neurons reciprocally (see *Artificial synapses*, Fig. 1B). At increments of 50μs of real time, the following steps were looped: 1) the biological membrane voltage was read from the electrode and used to calculate the synaptic current applied to the model neuron. 2) This current was applied to the model neuron as it was advanced through 50μs of simulation time. 3) The model membrane voltage was read and used to calculate the synaptic current applied to the biological neuron. 4) This current was applied to the biological neuron. Note that synaptic current was applied "continuously" to the biological neuron using the DCC mode of the Axoclamp amplifier. In step 4, this "continuously" injected current is updated to reflect changes in the presynaptic model neuron. When the model neuron was quiescent, the current delivered to the biological neuron was calculated to be zero. The time resolution of coupling was 50μs, which was effective to approximate real-time coupling for this system because biological variability of intrinsic period was relatively large and artificial synapses were sufficiently slow (see Fig. 2 for examples of rise time and fall time of

13

synaptic activation). Biological variability of intrinsic period was approximately 10% or 100ms for a typical burst period.

A. Unperturbed model neuron activity

B. Unperturbed biological neuron activty
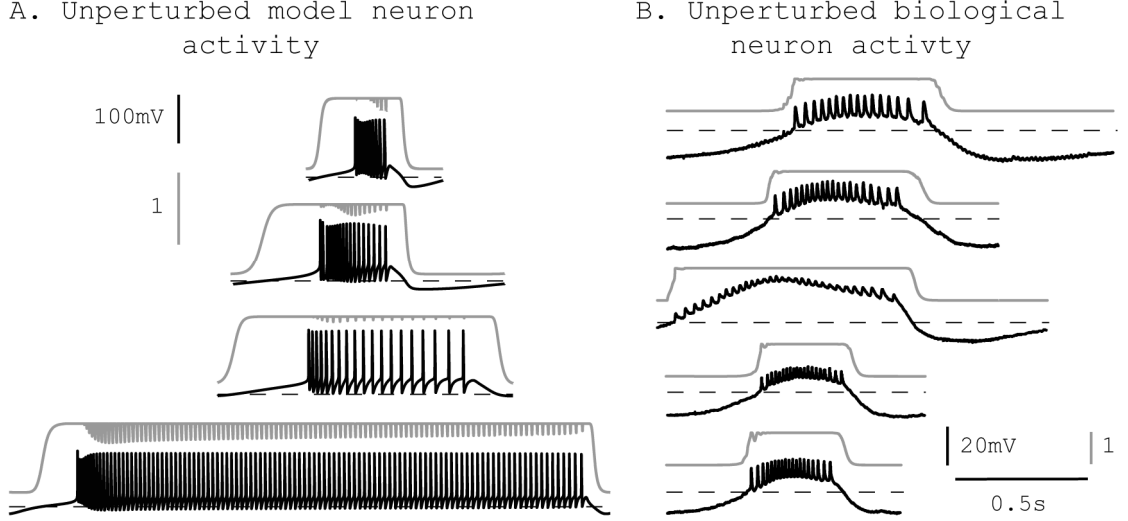
Figure 2. A,B: Snippets of free-running membrane voltage traces (black) and synaptic activation variables (gray) are shown for model neurons 1 to 4 (A, top to bottom) and for biological neurons 1 to 5 (B, top to bottom). Dashed lines show burst thresholds specific to each neuron. Timescale for both panels is shown in B. Synaptic activation variable *s* is unitless.

Artificial synapse

$$I_{syn} = g_{syn} \cdot s \cdot (V_{post} - E_{syn})$$
$$s = s_{inf} + (s - s_{inf}) \cdot e^{-\Delta t / \tau_s}$$
$$s_{inf} = (1 + e^{Vth - Vpre})^{-1}$$
$$\tau_s = \frac{1 - s_{inf}}{k_{min}}$$

We created hybrid networks by coupling one biological neuron to one model neuron via artificial synapses. Artificial synapses mapped the membrane voltage in one neuron to a synaptic conductance in its partner neuron, so bursts in the presynaptic neuron caused current to be injected in the postsynaptic neuron (Fig. 1B). For all artificial synapses implemented here, the synaptic current I_{syn} was calculated according to

14

a model of chemical synaptic transmission (Abbott and Marder 1999), where g_{syn} is the maximal conductance of the synapse, s is the synaptic activation, V_{post} is the membrane potential of the postsynaptic neuron, s_{inf} is the asymptotic value of s in time, Δt is the simulation timestep, τ_s is the synaptic time constant, V_{th} is the half-activation voltage of synaptic activation, V_{pre} is the presynaptic membrane potential, k_{min} is the backward rate constant of direct ligand binding to the ion channel, and E_{syn} is the synaptic reversal potential, which was set to 0mV for all synapses to make them excitatory. V_{th} and k_{min} were chosen so that the synapse was fully activated during a presynaptic burst and fully deactivated otherwise. For the networks presented here, $\Delta t = 50\mu s$, $k_{min} = 0.1ms^{-1}$ and V_{th} was set equal to the burst threshold of the presynaptic neuron (Fig. 2). Hyperpolarizations between spikes within a burst cause the model neuron voltage to drop below V_{th} during a burst. The synaptic time constant τ_s (which is controlled by the parameter k_{min}) acts as a lowpass filter, smoothing repeated crossings of V_{th} by the model neuron so that bursts are clear in the s trace. For each neuron, this threshold was chosen so that it was in the steepest part of the slow membrane voltage oscillation, giving the highest tolerance to baseline drift. The synaptic activation variable s varies between 0 and 1, so that the synaptic current I_{syn} is equal to the driving force (V_{post}-E_{syn}) scaled by a value between 0 and g_{syn}. Thus, when $s = 0$, the synapse is "off" ($I_{syn} = 0$), while when $s = 1$, the synapse is "on" and $I_{syn} = g_{syn}(V_{post}$-$E_{syn})$. Experimental values of g_{syn} varied from 1 to 10,000nS for the biological to model synapse and from 1 to 150nS the model to biological synapse. Model to biological synapse strength was limited by stability of the dynamic clamp (Preyer and Butera 2007).

Model neurons

In each hybrid network experiment we used one of four endogenously bursting model neurons, each a single compartment with eight Hodgkin-Huxley type membrane currents and an intracellular calcium buffer. The membrane currents were based on voltage-clamp experiments on lobster stomatogastric neurons (Turrigiano et al. 1995) and included a fast sodium current (I_{NaF}), a fast and a slow transient calcium current (I_{CaT} and I_{CaS}), a fast transient potassium current (I_A), a calcium-dependent potassium current (I_{KCa}), a delayed rectifier potassium current (I_{Kd}), a H-type current (I_H), and a leak current (I_{leak}). The model neurons differed only in the maximal conductances of their eight membrane currents; these conductances were chosen to produce different burst periods and duty cycles in the different model neurons (Fig. 2A). The model was described in detail in (Prinz et al. 2003). Model parameters are given in Table 1. The model was implemented in C^{++}, and all differential equations were integrated with the Exponential Euler Method (Abbott and Marder 1999) at a time resolution of 50µs.

Table 1. Model neurons used in this study. The form of these models is given in Prinz et al. (Prinz et al. 2003), and the maximal conductances for the eight membrane currents are given here.

Model Neuron	Maximal conductance (µS)							
	gNa	gCaT	gCaS	gA	gKCa	gKd	gH	gleak
1	251.32	0	6.28	12.57	6.28	15.71	0.03	0.01
2	125.66	0	6.28	6.28	12.57	62.83	0.01	0
3	251.32	1.57	3.77	25.13	6.28	47.12	0.03	0
4	188.49	3.14	6.28	0	6.28	47.12	0.03	0.02

PRCs

To make phase locking predictions for each of the 86 hybrid networks we present, we generated 172 PRCs, one for each neuron of each network. The PRC for each component neuron was constructed in open loop configuration (Fig. 1C,D) using a pulse in postsynaptic conductance that was elicited by a single spontaneous burst in the partner neuron and parameterized by synaptic strength. Other parameters of the artificial synapse were held constant. For example, to measure the PRCs of biological neuron 1 due to stimulus from model neuron 2 with synapse strength of 30nS, we first estimated what the profile of synaptic conductance received by the biological neuron would be in a closed loop network. To do this, we ran a simulation of the model neuron combined with the artificial synapse but isolated from the biological neuron. From this simulation we saved a snippet of the synaptic activation variable s. This snippet was equal to the length of one burst cycle of the model neuron, beginning at the start of a burst, where the synaptic activation variable s rapidly changed from 0 to 1, and ending with the quiescent interval of the neuron, where s was zero (Fig. 2A). To deliver a stimulus, this snippet of s was played into the artificial synapse, which defined the current injected into the biological neuron. The injected conductance was this snippet of s scaled by the maximal conductance of the synapse g_{syn}. Next, we determined the intrinsic period of the biological neuron, $P_{0,bio}$, from 20 consecutive periods of unperturbed activity. We defined $P_{0,bio}$ as the time between two successive crossings of a voltage threshold with positive slope. This burst threshold was equal to the synaptic parameter V_{th} so that the synaptic activation and burst thresholds were crossed simultaneously. The slow oscillation was isolated by filtering the voltage waveform according to

17

$V_{filt}(t+\Delta t)=V_{filt}(t)+(V(t+\Delta t)-V_{filt}(t))/\tau_{filt}$, where V_{filt} is the filtered waveform, Δt is the time step, and $\tau_{filt}=1ms$. For parity, the filtered voltage V_{filt} was used for all burst detection in both model and biological neurons. $P_{0,bio}$ was divided into 100 equally spaced stimulus intervals ts and 100 phase response trials were run. For each value of stimulus phase $\phi=ts/P_0$, ts is the delay from start of burst to start of stimulus, a stimulus is delivered and the phase response is measured. We define the first order phase response $F1(\phi)=(P_1-P_0)/P_0$, and the second order phase response $F2(\phi)=(P_2-P_0)/P_0$ where P_1 is the length of the cycle containing the stimulus and P_2 is the length of the subsequent cycle. In each trial, the stimulus was delivered at one value of ts, and the first and second perturbed periods $P_{1,bio}$ and $P_{2,bio}$ were measured. The recovery interval tr is the interval between stimulus onset and the next burst onset. Fig. 3 gives examples of stimuli delivered during the burst (Fig. 3A1 and square in subsequent panels), or immediately after the burst has ended (Fig. 3A2 and triangle in subsequent panels). The lower traces show the perturbation in conductance (snippet as in Fig 2A) driven by the model neuron. Burst onset as determined by burst threshold crossing was defined as phase zero $\phi=0$. Effects on the cycle containing the start of the perturbation were tabulated as first order resetting $F1$ (Fig. 3B1), and effects on the next cycle were tabulated as second order resetting $F2$ (Fig. 3B2). First and second order phase responses $F1$ and $F2$ were defined as the amount by which the respective cycle lengths $P_{1,bio}$ and $P_{2,bio}$ were extended relative to $P_{0,bio}$, and they were normalized by $P_{0,bio}$ (equations above). By this definition, a positive phase response value indicated a delay of the subsequent burst, while a negative value indicated an advance. To ensure that the biological neuron had returned to its unperturbed dynamical activity between stimuli, individual stimuli were delivered 4

18

cycles apart. To control for slow adaptation, stimuli were delivered in random order of stimulus phase. Fig. 3D shows how *F1* and *F2* are used to calculate equilibrium intervals *ts* and *tr*, denoted throughout this paper as ts^* and tr^*. These are intervals that can be observed in the presence of the repetitive stimulation that occurs in a closed loop network. As seen in the equations in Fig. 3D, the difference between *ts* in the open loop and ts^* in the closed loop is the *F2* term (see next section).
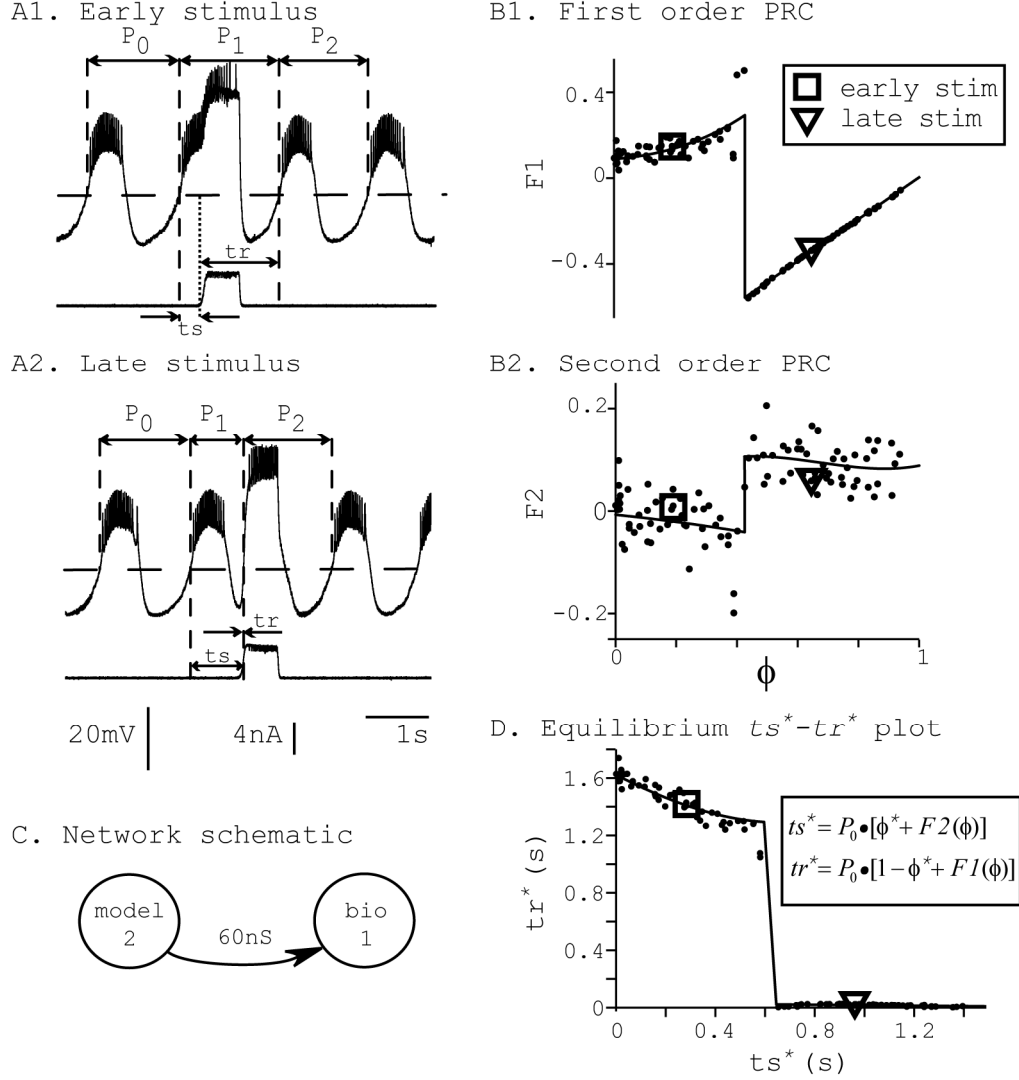
Figure 3. Example of PRC generation and equivalence of information in phase response curves vs. ts^*-tr^* plot. A: Membrane voltage traces (top) and injected current (bottom) showing the qualitative difference in response for a stimulus delivered during a burst (A1) vs. one delivered in the quiescent interval between bursts (A2). Dashed horizontal lines in A and B indicate burst thresholds. B: First and second order PRCs. Black dots denote phase responses measured from individual stimuli. Solid lines are piecewise polynomial fits. For first and second order PRCs, the order of polynomial fits ranged from 1 to 7 and 1 to 3, respectively. The locations of discontinuities were determined by inspection. Square and triangle marks the data point measured in panels A1 and A2, respectively. C: Schematic showing network connectivity used to measure these PRCs. D: Ts^*-tr^* curve calculated from *F1* and *F2* in panel B according to the given equations. This curve represents possible modes of 1:1 phase-locked activity for the biological neuron. The ts^*-tr^* curve is a parametric function of ϕ, as described in *Theoretical method*. Square and triangle marks the phase-locked mode calculated from the data marked in panels B1 and B2.

PRCs for the model neurons were generated post-hoc in an analogous manner. A

snippet of the free running biological voltage trace was used to calculate a snippet of the

synaptic activation variable *s*, which was saved and played into the artificial synapse to stimulate the model neuron. Again, to generate the PRCs *F1* and *F2*, this stimulus was applied at 100 equally-spaced intervals of the intrinsic period of the model neuron $P_{0,mdl}$.

Mean PRCs used in our analysis were estimated by piecewise polynomial fits to PRC data. The number of polynomial pieces used per PRC ranged from 1 to 3, and the order of these polynomials ranged from 1 to 7. The order of polynomial was chosen to be minimal while maintaining goodness of fit and correct end behavior. To estimate biological variability in the PRCs, envelopes marking the boundary of ± 2 standard deviations σ were constructed around each mean PRC. This was done by binning each PRC (N=5) and measuring σ at the center of each bin. Upper and lower envelopes were constructed using piecewise polynomial fits to the mean PRC±2σ. The number of polynomial pieces used to fit the envelopes was equal to that used for the mean PRC, and the order of polynomials used for the envelopes ranged from 1 to 3. The orders of polynomials used to fit envelopes were smaller than those used to fit mean PRCs because the binned data contained fewer data points.

Theoretical method

We used the theoretical methods of Oprisan, Prinz, and Canavier (Oprisan et al. 2004) to predict 1:1 phase-locking in hybrid networks from the PRCs of component neurons. This method first checks for the existence of 1:1 phase-locking using a periodicity criterion then checks that solutions are locally stable by analyzing a linearized version the system. Figure 4 shows the pulse coupled approximation upon which the theoretical method is based (periodicity criterion shown in 4A). Conduction delays are

ignored here, although they can be included in the approximation as shown previously (Oprisan et al. 2004; Woodman and Canavier 2008). Equilibrium stimulus phase ϕ^* and stimulus (recovery) interval ts^* (tr^*) are defined as ϕ and ts (tr) above, but in the context of an ongoing 1:1 phase-locked mode rather than a single input. Considering only first order resetting $F1_j$ of neuron j, ts^*_j and tr^*_j can be calculated as follows:

$$ts^*_j = P_{0,j} \cdot \phi^*_j$$
$$tr^*_j = P_{0,j} \cdot [1 - \phi^*_j + F1_j(\phi^*_j)]$$

In this case, where second order resetting is assumed to be zero, ts^*_j is the time elapsed between the start of the burst and the onset of input, and tr^*_j is the fraction of the cycle remaining before the next burst, calculated as $1 - \phi^*_j$ plus first order resetting. The quantities ϕ^*_j and $F1_j$ are unitless. We assume that each neuron returns to its unperturbed limit cycle before it receives a new input (see *Introduction,* third assumption). This is valid because the effects of each input are concluded during the perturbed cycle, before the next input is received, and there is no effect on the subsequent cycle ($F2_j$ is assumed to be zero). In Fig. 4B, *neuron 1* receives input during $P_1[n]$ after interval $ts_1[n]$. The first order effects of that input are incorporated during the interval $tr_1[n]$, and *neuron 1* is allowed to return to its limit cycle by the end of $tr_1[n]$. The effects of the input received during $P_1[n]$ are concluded by the time *neuron 1* receives the next input at the end of the interval $ts_1[n+1]$. When considering both $F1_j$ and $F2_j$, the calculation of tr^*_j is the same, however, $F2_j$ affects the subsequent cycle, so ts^*_j must be adjusted as follows:

$$ts_j^* = P_{0,j} \cdot [\phi_j^* + F2_j(\phi_j^*)]$$
$$tr_j^* = P_{0,j} \cdot [1 - \phi_j^* + F1_j(\phi_j^*)]$$

In this case, ts_j^* is adjusted to include second order resetting due to input in the previous cycle. Our third assumption is still valid because the next input is not received until ts_j^* is complete. The second order response of an input to a neuron causes the next cycle length to be lengthened or shortened. This effect is localized to the ts interval so that when that neuron receives its next input, it has returned to its limit cycle. Thus, the effect of F1 is localized to the tr interval of the current cycle, and the effect of F2 is localized to the ts interval of the next cycle.

A. Definition of intervals during phase-locking
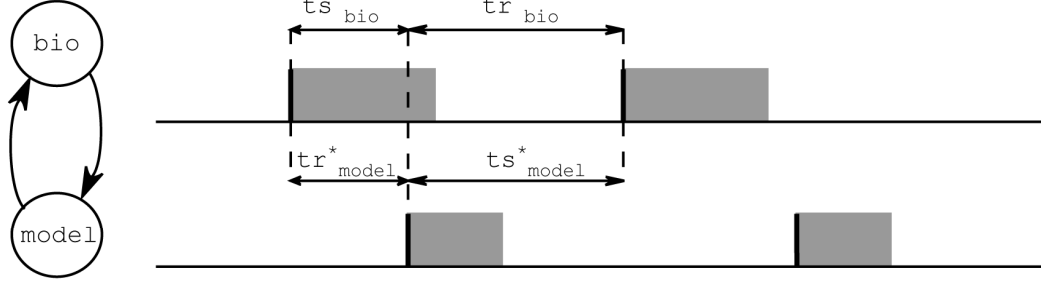
B. Convergence to a phase-locked mode
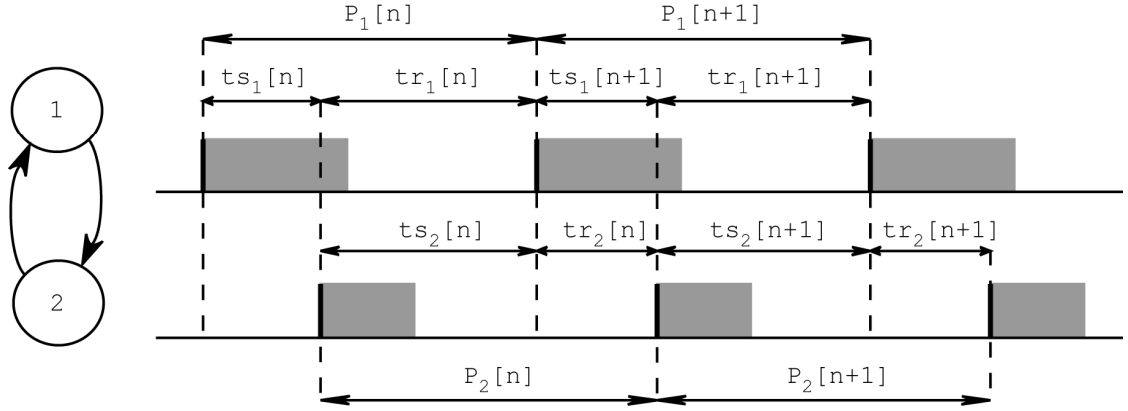
Figure 4. Pulse coupled approximation of a reciprocally coupled bursting network. Gray rectangles represent bursts. Equilibrium intervals ts^* and tr^* are defined in the text. Conduction delays are ignored. A: Definition of intervals during phase-locking between 2 neurons in closed loop configuration. For phase locking to occur, ts^* in the biological neuron (top) must be equal to tr^* in the model neuron (bottom) and vice versa. B: Convergence to 1:1 phase-locked mode. For a network to satisfy the stability criterion, this cycle-to-cycle mapping of $ts[n]$ and $tr[n]$ must converge to $ts_1[\infty]=tr_2[\infty]$ and $tr_1[\infty]=ts_2[\infty]$. This framework was used to derive a discrete map for the time-evolution of the system on a cycle-to-cycle basis. Figure adapted from (Oprisan et al. 2004).

We can solve for the existence of a 1:1 phase-locked mode using a periodicity criterion, which states that in a 1:1 locking the stimulus interval in one neuron is exactly equal to the recovery interval in the other: $ts^*_{mdl}=tr^*_{bio}$ and $tr^*_{mdl}=ts^*_{bio}$ (Fig. 4A). For a neuron j, any ordered pair (ts^*_j, tr^*_j) is uniquely determined by the phase ϕ^*_j when that neuron receives input, so these intervals can be considered functions of each other, i.e., functions f and g, $ts^*_j=f(tr^*_j)$ and $tr^*_j=g(tr^*_j)$, are both valid because ts^*_j and tr^*_j are themselves parametric functions of ϕ^*_j (Fig. 3D, equations). Thus, satisfaction of the

periodicity constraint can be evaluated graphically by plotting ts^*_{bio} vs. tr^*_{bio} and tr^*_{mdl} vs. ts^*_{mdl} (see *Example prediction of a 1:1 phase-locked mode in a hybrid network*). Considering the choice of axes, it follows that any intersection of the 2 curves gives $ts^*_{mdl}=tr^*_{bio}$ and $tr^*_{mdl}=ts^*_{bio}$. In other words, a phase-locked mode exists at any intersection.

Existence of a mode does not guarantee that it will be observed; it must also be stable, that is, robust to small perturbations. An intersection on a network's ts^*-tr^* plot uniquely defines a stimulus phase for each neuron, ϕ^*_{bio} and ϕ^*_{mdl} (as seen above). If the phase-locking defined by this point is also stable, then as cycle number $n \rightarrow \infty$, $\phi_j[n] \rightarrow \phi^*_j$. To test for stability, PRCs for each neuron are linearized around $\phi_j[\infty]=\phi^*_j$, and a return map is constructed that defines the evolution of a small perturbation ($\Delta\phi$) on a cycle-to-cycle basis. This map (Oprisan and Canavier 2001) is shown below, where n is the cycle number and $m_{i,j}$ is the linearized slope of the ith order PRC for neuron j at phase $\phi_j[\infty]$. Following this definition, $m_{2,j}$ is the slope of $F2(\phi_j[\infty])$.

$$
\begin{aligned}
\phi_j[n] &= \phi_j[\infty] + \Delta\phi_j[n], \\
\Delta\phi_j[n] &= ((1-m_{1,mdl}) \cdot (1-m_{1,bio}) - m_{2,mdl} - m_{2,bio}) \cdot \Delta\phi_j[n-1] - m_{2,mdl} \cdot m_{2,bio} \cdot \Delta\phi_j[n-2]
\end{aligned}
\tag{1}
$$

When $F2(\phi_j[\infty]) \neq 0$, two preceding cycles must be taken into account ($n-1$ and $n-2$), as shown above. Eigenvalues for this 2-D map are calculated as follows:

$$
\lambda^2 - ((1-m_{1,mdl}) \cdot (1-m_{1,bio}) - m_{2,mdl} - m_{2,bio}) \cdot \lambda + m_{2,mdl} \cdot m_{2,bio} = 0
$$

When both eigenvalues λ_1 and λ_2 are between -1 and 1, the system is stable.

Inclusion of noise in iterated firing time maps based on the PRC

We modeled a subset of our hybrid networks using the experimentally obtained PRCs of component neurons as well as their noise envelopes. For each component neuron *j*, interburst intervals (*IBI*) were calculated iteratively according to a modified Winfree model (Canavier et al. 1999).

$$IBI[n]_j = P_{0,j} \cdot \left[1 + \sum_{}^{k} F1_j(\phi_{j,k}[n]) + \sum_{}^{l} F2_j(\phi_{j,l}[n-1]) \right]$$

where P_0 is the intrinsic period, $\phi_{j,k}[n]$ is the phase at which neuron *j* receives the *k*th input in the current cycle, $\phi_{j,l}[n\text{-}1]$ is the phase at which the *l*th input was received by neuron *j* in the previous cycle, and *F1* and *F2* are polynomial fits of experimental PRCs modulated by Gaussian noise matching the distribution of experimental variability described by the envelopes of the appropriate PRCs. This map represents an ideal pulse coupled system. It differs from the map given in Equation 1 in that it does not assume a particular firing order. To construct each PRC, a Gaussian noise generator had output scaled to match the magnitude of the noise envelope and this noise was added to the PRC to within causal limits. Each iteration, a new amount of noise was added to the mean fit of the PRC, simulating the experimentally observed variability. To simulate a reduction in the overall amount of noise in the system, we scaled the noise envelope by a factor less than 1. The inclusion of noise in the PRC-based iterative map is similar to those of Netoff et al. 2005a; the major difference is the use of *F2* in addition to *F1* in our method.

Hybrid networks

We constructed 86 hybrid networks, each comprised of one biological and one model neuron coupled by artificial excitatory synapses via dynamic clamp (Fig. 1B). Each biological neuron was obtained from a different animal. Synapse strengths ranged from 1 to 10,000nS, a range that includes conditions of weak and strong coupling as can be verified by whether the PRCs scale linearly with respect to conductance (weak) or not (strong) (Preyer and Butera 2005). For each network, we verified the stable behavior of the biological neuron, then turned on the artificial synapses and recorded the membrane voltages of the biological and model neurons for at least 2 minutes. Most networks reached steady state within a few seconds. Only steady state data are reported here. These closed loop recordings were used to extract experimental values of phase-locked network period and relative phase.   Synaptic coupling forced some networks into a tonic firing regime. In these cases, we cut short the recording in order to avoid injecting a large amount of charge into the neuron.

Circular statistics

Circular statistics (Drew and Doucet 1991; Mancilla et al. 2007) were used to summarize observed hybrid network activity. This method allows the presentation of mean and variability of network phase as a single vector.   The angle of the vector represents mean network phase [Φ_{net} on the interval $(0, 1)$], and is given by

$$\tan\left(\frac{\pi}{2} \cdot (\Phi_{net} - 1)\right) = \frac{Y}{X},$$

where

27

$$X = \frac{1}{N} \sum_{k=1}^{N} \cos\left(\frac{2\pi \cdot ts_{j,k}}{P_{net}}\right),$$

$$Y = \frac{1}{N} \sum_{k=1}^{N} \sin\left(\frac{2\pi \cdot ts_{j,k}}{P_{net}}\right),$$

N is the number of bursts recorded in the experiment for neuron j, $ts_{j,k}$ is the stimulus interval for the kth cycle of neuron j, and P_{net} is the average network period. The strength of phase-locking is represented by the length of the vector, R, where $R^2 = X^2 + Y^2$. The threshold criterion $R^2 > 0.7$ was sufficient to separate networks in which phase locking was visually obvious from those in which it was not. Instantaneous network phase is represented by the ordered pairs (X_k, Y_k) so that in all circular plots shown, the angle $\Phi_{net} = 0$ is rightward, $\Phi_{net} = \frac{1}{4}$ is upward, $\Phi_{net} = \frac{1}{2}$ is leftward, and $\Phi_{net} = \frac{3}{4}$ is downward.

Results

PRC morphology

Many first order PRCs (*F1s*) measured from biological and model neurons had a characteristic shape that matched previous computational results for strong stimuli (Figure 3-D, Figure 5-A1-model, Figure 7-A1-biological, (Prinz et al. 2003; Maran and Canavier 2008). These PRCs had 2 branches separated by a discontinuity, where the phase response switched abruptly from large delay at early stimulus phases to large advance at late stimulus phases. Delay is defined as *F1>0*, and advance is defined as *F1<0*. The discontinuity falls at the point in phase where the neuron of interest ceases to burst and enters the quiescent interval. Stimuli delivered near this point in phase are either delivered during the burst, extending the burst and causing a delay (Figure 3-A), or immediately after the burst has ended, initiating a new burst and causing an advance

(Figure 3-B). The second order PRCs (*F2s*) corresponding to these *F1s* typically showed no effect for stimuli delivered during the burst and showed moderate delays for stimuli delivered during the quiescent interval. The direction of the effect of *F2* (delay) was counter to the direction of the effect of *F1* (advance), however, the magnitude of *F2* was always smaller than the magnitude of *F1* so that the total effect of resetting, taken as the sum of *F1(φ)* and *F2(φ)* for a given stimulus phase, *φ*, would always tend towards advance.

Figures 5-7 contain examples of the PRCs used in a typical accurate prediction (Fig 5) and in the two special cases that violated our assumptions: runaway excitation (Fig. 6) and noise-induced mode transitions (Fig. 7). Some *F1s* were "U" shaped and always advancing (Figure 5-A1-biological). This occurred when the stimuli delivered during the burst were too weak to extend the burst. Because the stimuli were long, some stimuli with onsets during the burst did not offset until significantly after the burst had ended, and these "tail" intervals caused the neuron to speed up or advance in phase. As the stimulus onset was incrementally shifted later within the duration of the burst, there was an incrementally longer tail interval after the end of the burst where the stimulus remained on, causing incrementally larger advances in phase. This is seen in the PRC in Fig. 5A1 as a region where *F1*<0 and where the slope of *F1* is negative. The boundary of this effect was where stimulus onset was at the end of the burst. Beyond this boundary, stimuli were sufficiently strong to initiate a new burst, causing an advance in phase along the causal limit of the PRC. This causal limit corresponds to *tr=0*, and is seen in the PRC as the line *F1(φ)=φ-1*. The "U" shape was less evident in the model neuron shown in Fig. 7A1 due to saturation of the tail region's phase-resetting effect. For this PRC, the

burst length (0.3s) was much shorter than the stimulus duration (0.8s), which caused the tail region to be large for all stimuli with onsets during the burst so that the magnitude of the advance was essentially independent of phase during the burst. This was not the case for the biological neuron in 5A1, because the duration of the stimulus was similar to that of the burst, such that the duration of the interval between burst offset and stimulus offset increased from essentially zero at zero phase to essentially the stimulus duration near the end of the burst, resulting in a significant dependence of the magnitude of the phase advance on phase during the burst. These results are consistent with the results of Prinz et al. (Prinz et al. 2003).

Some *F1s* exhibited a flat region at very early phase, as seen in Figure 6A1-biological. This corresponded to stimuli that were delivered entirely during an endogenous burst, beginning during a burst and ending before that burst would have terminated on its own. On the other hand, stimuli whose onset occurred during the burst but whose offset occurred after the burst would have terminated normally extended the burst, causing a delay.

F1s obtained from model neuron 4 using strong stimuli showed advances at early phase (data not shown). In these cases, stimuli delivered during the burst increased spike frequency, and the burst was truncated at the offset of the stimulus. The interburst interval remained constant, resulting in an overall advance in phase. Stimuli delivered at late phases initiated a burst immediately, causing an advance in *F1*. These stimulus-derived bursts also exhibited increased spike frequency and had a shortened burst length. Because the subsequent quiescent interval was of typical length, the net effect was an advance in *F2*. The mechanism underlying these PRCs has been described as "complete

reset" (Benson 1980; Maran and Canavier 2008) because no matter at what phase the stimulus is applied (old phase), the phase after the stimulus (new phase) appears to be constant.

In Figure 6A2-model and Figure 7A2-model, *F2* was advancing late in phase because the duration of stimulus was longer than the burst length. For stimuli delivered late in phase, the stimulus was delivered during the quiescent interval, remained on during the subsequent burst, and remained on for a short interval after the burst had ended. During the last interval, the neuron was sped up, causing an advance in *F2*. This phenomenon is consistent with the emergence of a distinct limit cycle during the stimulus (Glass and Winfree 1984; Maran and Canavier 2008).

Many of the PRCs we obtained appear to have multiple discontinuous branches. The first and second order phase resetting curves can be discontinuous because of threshold effects (Glass and Winfree 1984) or shifting frames of reference. The apparent discontinuity at zero and one stems from a shifting frame of reference. In other words, the points 0 and 1 are identical in the phase space except for their frame of reference- the exact same resetting occurs, but at a nominal phase of 0 the reset is attributed to the first cycle whereas at a phase of 1 it is attributed to the second cycle. This is not a true discontinuity, so the sum of all resetting should be continuous at zero and one. Third order resetting (*F3)* was negligible for all neurons. For a more detailed review and phase-plane analysis of the types of PRCs shown here, see (Maran and Canavier 2008).

Example prediction of a 1:1 phase-locked mode in a hybrid network

A typical successful prediction of phase-locking is shown in Fig. 5. Data points from the first and second order PRCs for the biological neuron (red dots) were fitted with polynomials (Fig. 5A) and those for the model neuron (blue lines) were generated numerically. These PRCs were used to calculate the ts^*-tr^* curve for each component neuron (Fig. 5B). The existence of any 1:1 phase-locked modes was determined graphically as the intersections of these curves (Fig. 5B). Noise in the biological neuron was caused primarily by variability in the intrinsic period. The effects of this noise were incorporated in our prediction method by creating an envelope (dashed lines) around the biological PRC and mapping it to the ts^*-tr^* plot, as was done for the mean PRCs. In this example, there are two intersections on the ts^*-tr^* plot (blue indicates model tr^* as a function of ts^*, red indicates biological ts^* as a function of tr^*), indicating the existence of two modes of phase-locking (Fig 5B). Our calculations predicted that phase-locking would be stable only at one intersection (arrow). This predicted stable mode of phase-locking was mapped back to phase in the component neurons and indicated using appropriately colored arrowheads (Fig. 5A, arrows).
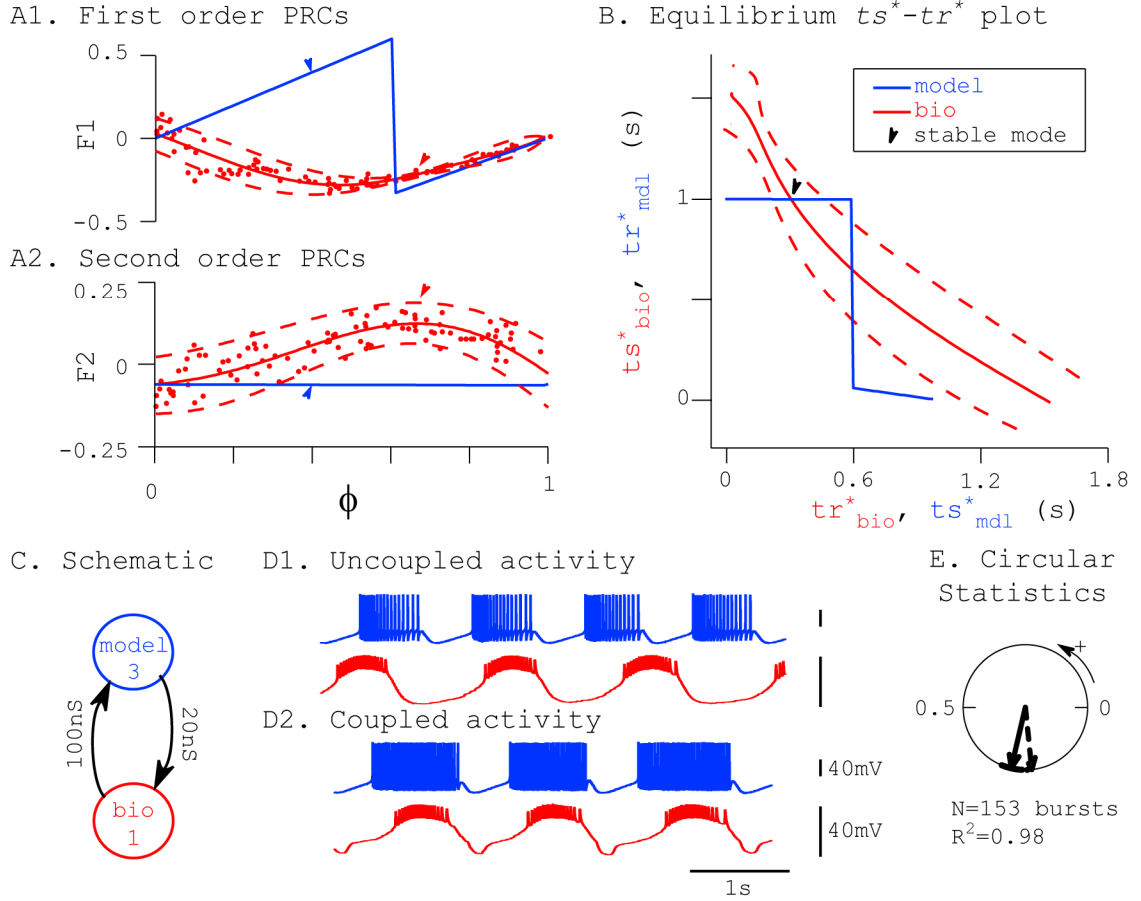
Figure 5. Example of a good prediction. A: Phase response curves (PRCs) obtained in open loop configuration from the model (blue) and biological (red) neurons. Raw data points from the biological neuron's PRC are shown, along with a polynomial fit and upper and lower envelopes at $\pm 2\sigma$ (dashed lines). Colored arrows indicate stimulus phases for each neuron where the stable mode of synchrony is predicted (see arrow in Panel B). B: Graphical method for determining existence of a 1:1 phase-locked mode (ts^*-tr^* plot). Parametric curves of ts^* vs. tr^* for model (blue) and biological (red) neurons are shown. Dashed lines indicate an envelope around the biological curve of $\pm 2\sigma$. Intersections reveal points where 1:1 phase-locked modes exist; out of two such points, one was calculated to be stable (arrow). C: Schematic specifying the hybrid network. Model neuron 3 was coupled to biological neuron 1 using artificial synapses with maximal conductances (g_{syn}) as shown. PRCs were measured in open loop configuration using stimuli scaled by g_{syn} as described in *Methods*. D: Uncoupled (D1) and coupled (D2) network activity. E: Circular statistics. Dots along the perimeter of the circle represent instantaneous network phase, defined post-hoc as $ts_{bio}/P_{network}$ (see *Circular statistics*). We predicted a mode of phase-locking at $\Phi_{network}=0.77$ (dotted arrow), and we observed a mode of phase-locking in this hybrid network at $\Phi_{network}=0.71$ (solid arrow).

In Fig. 5D, we show uncoupled (D1) voltage traces, then turn on the coupling as in Fig. 5C and show the stabilized locked mode after the transients dissipate (Fig. 5D2). Although the coupled neurons have a phase difference of nearly a quarter cycle

33

considering only burst initiation as a reference point, the overlap between the spiking and nonspiking phases is nearly maximal considering that the duty cycles, or fraction of the cycle comprised by the burst, is different. Thus the phase lag alone is not a complete measure of the degree of synchronization. The burst lengths of both neurons changed when they were coupled. Although this violated our second assumption, that the shape of synaptic inputs received in the closed loop network are equal to those used in open loop configuration to measure the PRC, our methods appear robust to the amount of variation in burst length shown.

In Fig. 5E, we describe coupled activity using circular statistics. Data points along the perimeter of the circle represent network phase on each cycle, defined as $ts_{bio}/P_{network}$. Phase-locking was tight in this example, so these data points blur into a thickening of the circle. We predicted a mode of phase-locking at $\Phi_{network}=0.77$ (dotted arrow), and we observed a mode of phase-locking in this hybrid network at $\Phi_{network}=0.71$ (solid arrow). In this case, the envelope of the biological ts^*-tr^* curve is sufficiently narrow and the intersecting branch of the model ts^*-tr^* curve is sufficiently wide that the mean and both envelopes of the biological neuron's ts^*-tr^* curve each have one stable and one unstable intersection with the model ts^*-tr^* curve on the intersecting branch. For this reason, we expect the phase-locked mode to be robust to biological noise.

Summary of qualitative predictions

Our goal was twofold – first, to accurately predict 1:1 phase-locking in hybrid networks of bursting neurons coupled by excitatory synapses, and second, for those networks exhibiting phase-locking, to predict the phase-locked period and network phase.

A summary of results relating to our first goal is shown in Table 2. We constructed 86 hybrid networks using 5 biological neurons and 4 model neurons. Excluding 17 networks that violated our assumptions (special cases), our method correctly predicted whether a stable one to one locking would be established in 66 networks, a success rate of 96%. In three cases only, either a stable 1:1 locking was predicted but not observed, or observed but not predicted. When our method was simplified to utilize only $F1$, as opposed to $F1$ and $F2$, the success rate was reduced to 82%.
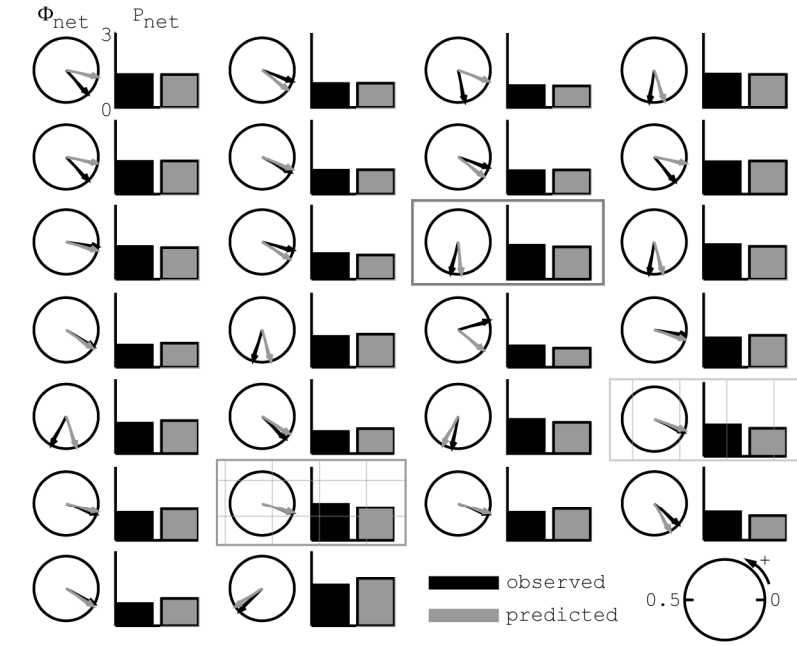
Table 2. Summary of qualitative predictions. Qualitative summary of predictions of 1:1 phase-locking using first and second order phase response curves (*F1* and *F2*). Each cell represents one hybrid network. Each network is defined by one model neuron (column 1), one biological neuron (column 2), and the maximal conductances of their artificial synapses (columns 3 and 4-12). Classifications of observed and predicted network activity are coded and displayed as "observed"/"predicted," where a network may be observed to exhibit one of 3 types of behavior: 1:1 phase-locking ("a"), no phase-locking ("-"), or higher modes of phase-locking, which we call complex modes ("c"). Networks of interest are marked by a symbol following a comma; they are runaway excitation (RE), noise-induced mode transitions (N), and depolarization block (DB). These are discussed in the text. Individual networks are also color coded according to the accuracy of our method in predicting the observation of phase-locking. Cells are colored green to indicate that our method was successful, red to indicate failure, and yellow to indicate failure under special circumstances (see *Special Cases* for further explanation).

Model Neuron	Biological Neuron	$g_{model>bio}$ (nS)	$g_{bio>model}$ (nS)								
			1	10	20	30	60	80	100	300	10000
1	3	30	-/-			-/-			-/a		a/a, DB
1	3	100	-/-			-/-					
1	4	10	-/-	-/-		c/-			a/a		
1	4	30	-/-	-/-		c/-			a/a		
1	5	10	c/-	-/-		-/-			-/-		-/-
1	5	30	c/-	-/-		-/-			c/-		
2	1	20	-/-	c/-	a/-		a/a	a/a	a/a		
2	1	60	c/-	-/-	-/-		-/-				
2	2	30				a/a			a/-, N		a/a
2	2	60	-/a, N			a/a					a/a, DB
2	2	150	a/a								
2	5	10	c/-	c/-		c/-			c/-	c/-	-/-
2	5	30	c/-	c/-		c/a			a/a		
2	5	100	c/a, N	-/-		-/a, RE			-/a, RE		
3	1	20		a/a			a/a	a/a	a/a		
3	2	30				a/a					
3	4	10	a/a	a/a					a/a		
3	4	30	a/a	a/a		a/a			a/a		
3	4	100	-/-	-/a, RE, N		-/a, RE			-/a, RE, N		
3	5	10	c/-	c/a, N		c/a, N			c/a, N		
4	3	30	-/-			-/a, RE, N			a/a		
4	5	10	-/a, RE, N	-/a, RE					a/a		
4	5	30	a/-, N	-/-					-/a, RE		
4	5	100	a/a	-/a, RE, N					-/-		

36

Summary of quantitative predictions

In addition to predicting the mode of activity in hybrid networks, we predicted phase-locked period and network phase. For the 26 networks that were both predicted to phase-lock and exhibited phase-locking, we show a circular phase plot and a bar plot for each network (Fig. 6A). For all networks, predicted values of phase-locked network phase (Fig 6B1) and period (Fig 6B2) are accurate to within the experimental variability observed in the biological neuron's intrinsic period. Most observed modes of activity show the model neuron leading the biological neuron (black arrows in the bottom half of the circle). The two hatched boxes indicate networks that exhibited phase-locking due to depolarization block (see *Phase-locking mediated by depolarization block in the model neuron*).

Figure 6. Quantitative summary of observed and predicted 1:1 phase-locking in hybrid networks. A: Each pair consisting of one circular plot and one bar plot represents one hybrid network where 1:1 phase-locking was both predicted and observed. Circles show the observed (black) and predicted (gray) network phase, which is defined between 0 and 1. A network phase of zero, $\Phi_{net}=0=1$, is shown as a rightward arrow, and phase is increasing in the counter-clockwise direction. Observed network phase is calculated as the mean of ts_{bio}/P_{net}. Predicted network phase is calculated from the ts^*-tr^* plot as $ts^*_{bio}/(ts^*_{bio}+ts^*_{mdl})$. Bars show the observed (black) and predicted (gray) network period P_{net}. All bars are on the same scale, with the scale bar equal to 3s. The hybrid network shown as an example in Fig. 5 is boxed in gray, the network showing depolarization block (DB) in Fig. 10 is cross hatched and another network that exhibited DB is vertically hatched. These plots are on a grid ordered from left to right, top to bottom by ascending absolute difference between the predicted and observed network period. B: Summary plots of predicted vs. observed values of network period (B1) and network phase (B2). Dotted lines give an envelope of +/- 10% of the network period.

38

Runaway excitation

Special case #1- runaway excitation (denoted by "RE" in Table 2) - coupling was effectively continuous. This occurred when either synapse was continuously active during coupled activity. This was often caused by reciprocal excitation in combination with large synapse strengths and a tonic firing mode in at least one neuron. The tonic firing mode in this case represents oscillator death with respect to the bursting limit cycle (Ermentrout and Kopell 1990). Our method assumes pulsatile coupling, specifically that the stimulus received in closed loop approximates that used in open loop to construct the PRCs. For networks that have continuously active synapses, our methods are not valid. These networks were marked with the letters "RE" in Table 2. An example is shown in Fig. 7. We applied our methods as seen above (*Example prediction…*). Although our methods predicted a 1:1 phase-locked mode, reciprocal excitation in the coupled network caused the model neuron to fire tonically and depolarized the biological neuron to above its threshold of synaptic activation (D). Both synapses were continuously active. When the neurons were coupled, the model neuron was not able to return to its unperturbed limit cycle between perturbations (*Introduction*, third assumption), which explains why our methods made an incorrect prediction.
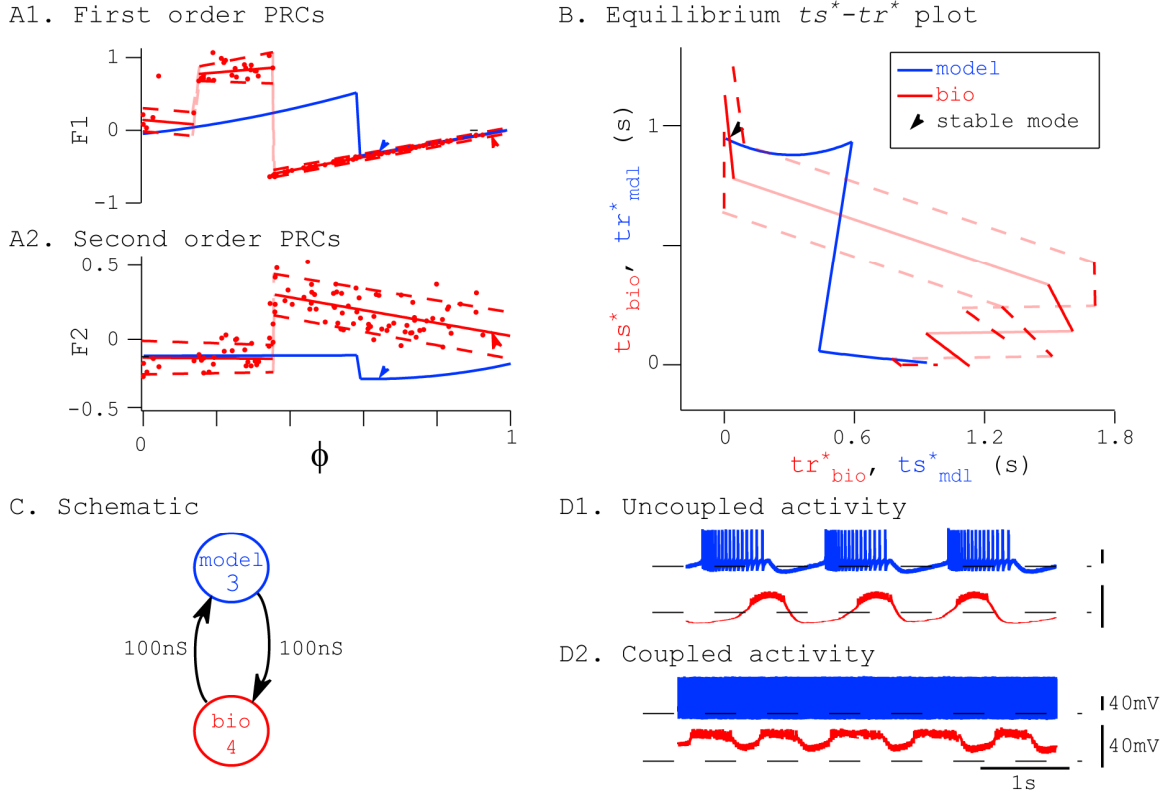
Figure 7. Example of runaway excitation- A: PRCs. B: Ts^*-tr^* plot. For clarity, line segments connecting discontinuous branches of the PRCs are shown as semi-transparent lines. C: Network schematic. D: Network activity. Dotted lines are at the half-activation thresholds for artificial synapses with respect to their pre-synaptic neurons. The prediction procedure illustrated in this fig. is the same as the one described in the legend for Fig. 5.

Noise induced transitions

Special case #2- noise-induced mode transitions (denoted by "N" in Table 2) - complex behavior resulted from a discontinuous PRC. This criterion was satisfied when biological noise, as visualized by an envelope around the biological ts^*-tr^* curve, was large enough to cause the existence of a phase-locked mode to appear or disappear. An example is shown in Fig. 8. Measured PRCs and envelopes (A) were again used to calculate values of ts^* and tr^* (B) for each component neuron used to construct the network (C). The periodicity constraint was solved graphically (B), and a stable phase-

40

locked mode was predicted to exist (arrows, A, B); however, observed coupled activity was complex. This network was active in what could have been a 2:1 mode, seen in raw traces (D) and in circular statistics (E) as one loose and one tight cluster of points around the circle. In this case we defined network phase relative to the model neuron so that no bursts would be ignored, $\Phi_{network}=ts_{mdl}/P_{network}$. Note the large noise envelope around the biological curve in the ts^*-tr^* plot (B, dashed lines). In contrast to the intersection of the ts^*-tr^* curves in Fig 5B, the intersection on Fig 8B is not structurally stable, because the upper and lower envelopes of the bio ts^*-tr^* curve do not intersect with the model ts^*-tr^* curve as does the mean fitted curve. Often, this is equivalent to saying that the intersection is close to the discontinuity, meaning that they are both within the noise envelope. In this case, a small deviation of the mean biological PRC (solid line) within this envelope would be sufficient to cause the intersection of the two ts^*-tr^* curves to disappear. Intersections represent fixed points in phase space. When they are created or annihilated, a bifurcation has occurred in the system. If the presence of noise, as quantified by the upper and lower envelopes of the measured PRC, can create or annihilate a fixed point, then the prediction is a complex phase walk through mode (Ermentrout and Rinzel 1984) rather than a one to one locking.
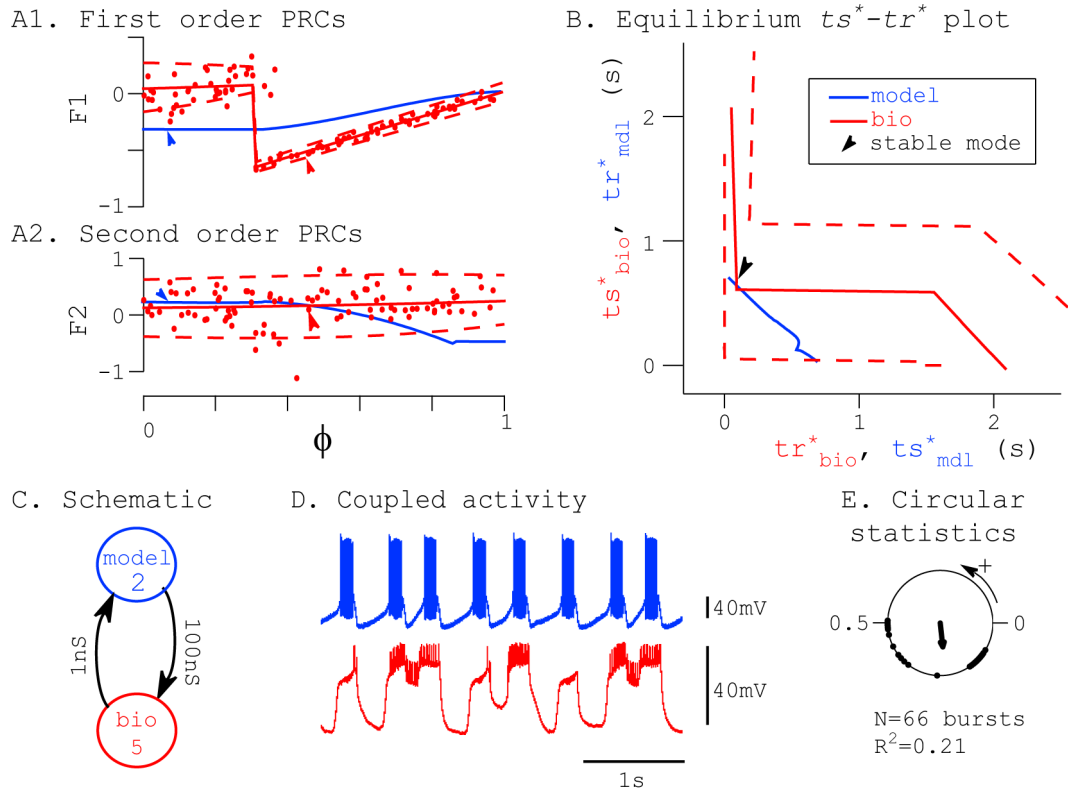
Figure 8. Example of noise-induced mode transitions. A: PRCs. B: Ts^*-tr^* plot. C: Network schematic. D: Coupled activity. E: Circular statistics showing complex behavior. The prediction procedure illustrated in this fig. is the same as the one described in the legend for Fig. 5.

The iterated map described in the methods determines the timing of future spikes based on the PRCs and the timing of previous spikes. The sensitivity of the bifurcations described above to a noise was explored using the iterated map (Fig. 9). Fig. 9A shows the circular statistics for a robust example taken from Fig. 5 (A1) and a sensitive one taken from Fig. 8 (A2). The major difference in the observations (thick black arrows) is that the one for the robust case has unit length (touches the unit circle) indicating a robust locking with an R^2 near one whereas the one for the sensitive case falls far short of the length (R^2) of 0.7 that was designated in the methods as the cutoff for a robust locking. At low noise levels (1% of the measured noise levels), the firing intervals produced by the iterated map produced robust 1:1 locking as indicated by the thin gray arrows that

nearly touch the unit circle and that match the predictions of graphical method based on the PRC (stars). On the other hand, when the noise is increased to 100% of the measured levels, there is a clear distinction in the output of the iterated map for the robust and sensitive cases. The circular statistics of the iterated map with the higher noise level (thin black arrows) are similar to the lower noise level case in A1 (thin gray arrow), but in A2 the thin black arrow has length near zero, indicated the absence of 1:1 locking, and is not visible. For clarity, the output of the iterated map is only shown at two noise levels in Panel A, but in Panel B, bar plots of R^2 values are summarized for several simulations. The magnitude of R^2 is nearly flat in B1, reflecting the insensitivity to noise of the robust prediction. On the other hand, the magnitude of R^2 falls off sharply in B2 when the noise becomes large enough to elicit bifurcations. For nominal noise levels, the simulations matched experimental observations, predicting phase-locking to occur (B1, asterisk) or not (B2, asterisk). This is a clear demonstration of the power of PRCs to predict the behavior of the networks in the presence of noise. In this example, noise induces transitions between 1:1 locking and phase walk through (Ermentrout and Rinzel 1984), which can be predicted from ts^*-tr^* plots by considering the noise envelope. We can only predict a 1:1 phase-locked mode with certainty (as seen in Fig. 5B), when the model ts^*-tr^* curve crosses the entire biological ts^*-tr^* envelope, dividing it into 2 distinct areas. Those networks in which the model ts^*-tr^* curve intersects with only a portion of the biological ts^*-tr^* envelope are sensitive to noise and were designated as special cases of the bifurcation type, noted in Table 2 with the letter "N." These cases required an extension of the original methods, which assumed that the presence of noise did not

43

qualitatively alter the dynamics, but are within the scope of the methods as extended here.
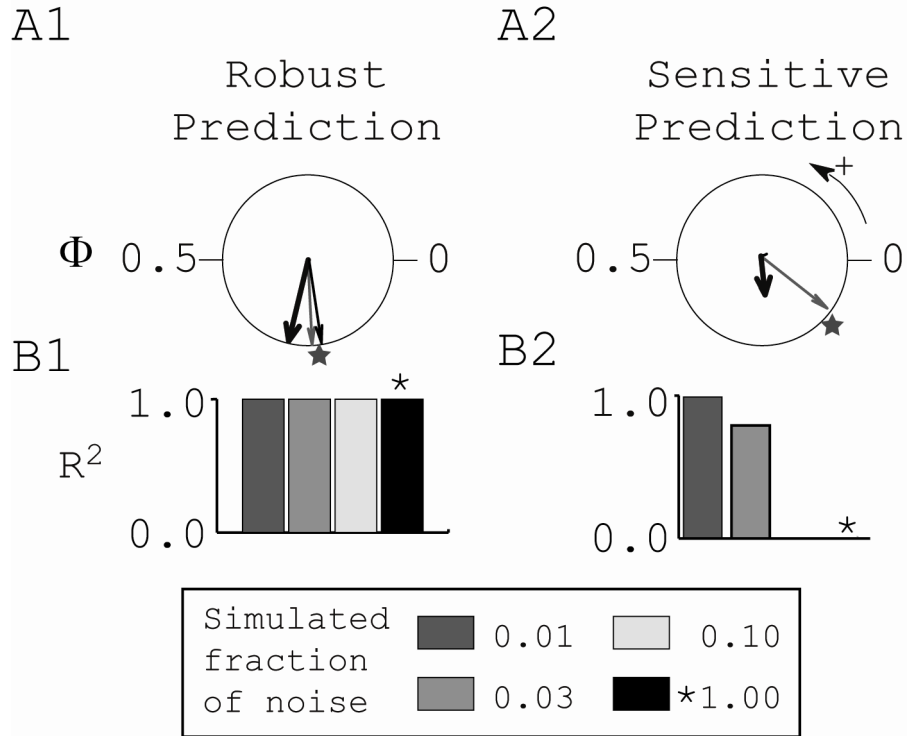
Figure 9. Effects of noise parameter in iterated map based on PRCs. A: Circular statistics. Thick arrows show experimental observations; stars, predicted network phase; thin arrows, iterated map results. B: R2 vs. simulated fraction of experimentally observed noise. Noise envelopes from biological PRCs were scaled by the values shown and used in the iterated map. Values of R2 summarizing the strength of 1:1 phase-locking seen in the iterated map are shown. A1, B1 based on data shown in Fig. 5. A2, B2 based on data shown in Fig. 8.

Phase-locking mediated by depolarization block (DB)

Phase-locking mediated by depolarization block (DB) in the model neuron (denoted by "DB" in Table 2). In a subset of hybrid networks, we observed 1:1 phase-locking that was mediated by depolarization block (DB) in the model neuron. Quantitative predictions for an example network (Fig. 10C) were obtained using the PRCS in Fig 10A and the tr^*-ts^* plots in Fig. 10B. Surprisingly, these predictions are

reasonably accurate, as summarized in Fig 10 E. and the cross hatched panel in Fig. 6. This is despite the fact that the model neuron (blue in Fig. 10D2) never drops below the activation threshold (horizontal dashed line) in the coupled network, and has a different waveform than in the uncoupled case (D1). An explanation of how the locking occurs is as follows. When coupled, the biological neuron drives the model neuron into DB during the biological burst. At the end of the biological burst, the model neuron is released and begins a burst after a short delay. This model burst excites the biological neuron, which initiates a burst and re-starts the network cycle by causing DB in the model neuron once again.
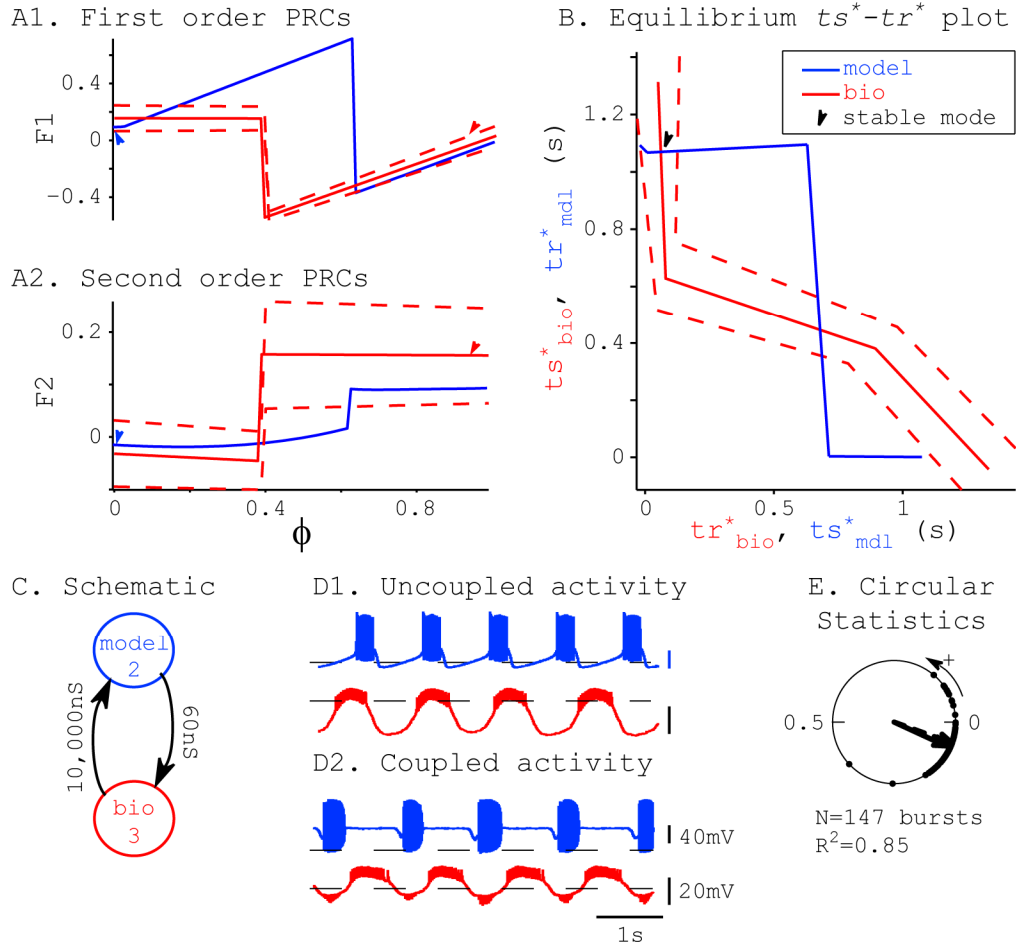
Figure 10. Prediction of phase-locking via depolarization block. A: PRCs. B: Ts^*-tr^* plot. C: Network schematic. D: Network activity. Dotted lines are at the half-activation thresholds for artificial synapses with respect to their pre-synaptic neurons. E: Circular statistics showing strong phase-locking. The prediction procedure illustrated in this fig. is the same as the one described in the legend for Fig. 5.

Discussion

Generality of our method

In order to predict the activity of two coupled oscillators, we require no knowledge of their intrinsic dynamics and no limitations on coupling strength, but only need to be able to measure PRCs from each oscillator. The assumptions we made were: 1) Each neuron is a limit cycle oscillator; 2) The shapes of synaptic inputs received in the

closed loop network are equal to those used in open loop configuration to measure the PRC; 3) In the closed loop network, each neuron returns to steady state (its unperturbed limit cycle) before it receives a new synaptic input; and 4) The AB/PD complex can be treated as a single oscillator, or neuron.

1) Each neuron is a limit cycle oscillator, meaning here that it has oscillatory bursting and exactly reproducible steady state behavior. Jitter in the dynamic clamp hardware caused the update interval of the model neurons to vary around 50μs (Dorval et al. 2001), however, we did not observe variations in the intrinsic period or duty cycle of the model neuron. A constant intrinsic period was assumed for both neurons, but the biological neuron's intrinsic period varied by ~10%. This variability was manifested as noise in the biological PRCs and was the main source of error in our results. Because these experiments were done using biological neurons whose function may benefit from variability (Hooper 2004; Horn et al. 2004), we hypothesize that the same methodology would produce fewer special cases if applied in a system that would not benefit from variability. 2) The shapes of synaptic inputs received in the closed loop network are equal to those used in open loop configuration to measure the PRC. We observed that burst durations in closed loop differed from those in open loop (Figs. 5, 7, 8, 10). This introduced some error, but it did not correlate with observed prediction errors. 3) In the closed loop network, each neuron returns to steady state (its unperturbed limit cycle) before it receives a new synaptic input. Slow drift of the biological intrinsic period between the time when PRCs were measured and the time when hybrid networks were connected introduced error into the phase predictions of hybrid networks. We measured third order resetting $F3=0$ in all neurons, nonetheless it is possible that adaptation of slow

variables in the biological neuron could introduce error into the predictions of phase-locked period and network phase. Our PRC measurement did not account for adaptation, but a variant of this methodology (Cui et al. 2008) can account for adaptation where necessary. 4) The AB/PD complex can be treated as a single oscillator, or neuron. We impaled PD cell bodies in four preparations and the AB cell body in one preparation, whereas the oscillator kernel is presumed to be in the neurites of the AB neuron. Although the location of our electrode was some physical distance from the presumed location of the kernel, we found no evidence that space clamp was an issue in any of the preparations.

The observation of phase-locking was correctly predicted in 96% of 70 networks, excluding seventeen networks that fell into two special categories described in the next section. Further, in the cases where phase locking was both predicted and observed, our quantitative predictions of network phase and phase-locked period were accurate within experimental variability. The overall success of our method despite the large amount of variability inherent in biological systems indicates that it is likely that this method can be applied to gain insight into a variety of biological circuits in which the appropriate PRCs can be measured.

Successful prediction of networks exhibiting phase-locking via depolarization block

DB has been previously reported as a mechanism of phase-locking, specifically for switching between 1:1 and 1:2 entrainment in the lobster stomatogastric nervous system (Robertson and Moulins 1981). DB has been also been observed as a mechanism patterning neural activity in rat hippocampal slices. Ziburkus et al. observed DB in

oriens interneurons due to excitatory input from pyramidal neurons during seizure like events, describing it as a novel pattern of interleaving activity (Ziburkus et al. 2006). In our results, the two networks exhibiting DB were accurately predicted in Table 2 (marked as DB) and Fig. 6 (shown by vertical and cross hatches) despite the unusual nature of this phase-locked mode. This is possible because, using our PRC protocol, inputs applied to the neuron cause phase delays that can be used for prediction regardless of whether the neuron is hyperpolarized or in DB during the delay.

Systematic prediction failures observed for excitation but not inhibition

The analysis of circuits coupled by excitation provides an interesting contrast to that of the analysis of circuits coupled by inhibition. Previously, we showed that our theoretical methods predict 1:1 modes of phase-locking robustly, where 161 out of 164 networks were predicted correctly (Oprisan et al. 2004). In contrast to the uniform success we experienced with inhibitory circuits, a significant fraction of the hybrid circuits constructed with excitation suffered from prediction failures. Most of these failures fell into two broad categories: runaway excitation and noise-induced transitions. In the runaway excitation case, synaptic coupling was strong and positive feedback in the network caused at least one neuron, usually the model neuron, to be tonically active. Tracking changes in burst length as well as cycle length due to coupling may allow prediction of tonic spiking in the coupled circuit (Oprisan and Canavier 2005)(and below).

One strong synapse doesn't support runaway excitation. Both synapses have to be strong. Since our model neurons were easily sent to tonic spiking, it was the model-to-bio

synapse strength that appeared to be most important in our data, however, it was necessary for both synapse strengths to be "sufficiently strong." Fig. 11 shows an example of a sufficiently strong model-to-bio synapse. During input I_{syn} (gray trace), V_{bio} (black trace) remains above threshold (dashed line). Fig. 11B shows a synapse that is too weak to support runaway excitation. These traces from PRC measurement protocols are representative of the super- or sub-threshold activity of the bio neuron while receiving strong or weak input, respectively. It was necessary for both the model PRC and the biol. PRC to exhibit this behavior in order for runaway excitation to occur. This is one way we could determine a priori which networks would succumb to runaway excitation.
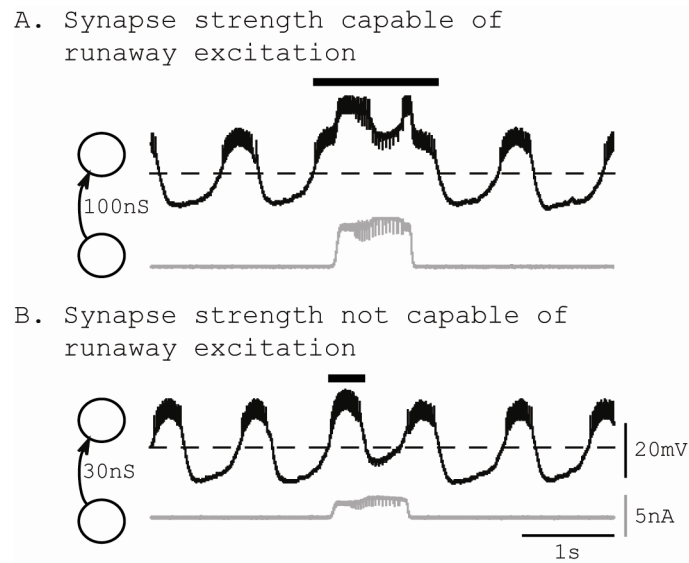
Figure 11. Critical strength of synapse for runaway excitation. Each panel shows the effect of one open loop stimulus from a partner model neuron (gray traces) on a free-running biological neuron (black traces). A: The model-to-bio synapse (100nS) extends the bio burst significantly (thick black bar), as determined by the burst threshold (dashed line). B: The model-to-bio synapse (30nS) does not extend the bio burst (thick black bar).

An implicit assumption in our previous work was that the presence of noise would not qualitatively change the mode expressed. In this study, we improve the prediction

methods by identifying cases in which the presence of noise will make a qualitative difference. This is a significant extension of the method to real noisy systems. Essentially, noise in a biological PRC can cause an intersection on the ts^*-tr^* plot to transiently appear or disappear. The structural instability appears to be correlated to the presence of two or more branches in the first order PRC for excitation, and consequently in the ts^*-tr^* curves. The presence of multiple branches was not generally observed for inhibition.

Validation of the PRC map method in reproducing structural instability

In a strong validation of our methodology, a map of the firing times in the network including noise verifies that variability in a PRC does modulate the strength of phase-locking. When noise was added to the map in a biologically plausible way, the differential effects of noise on structurally stable and unstable systems was captured qualitatively and quantitatively using circular statistics. This simple idea is a powerful tool for understanding the predictive utility of PRCs because it simulates the measured variability of the biological neuron and gives outputs that are readily compared to experimental data. The structural stability depends upon the ratio of noise, or variability, to the strength of the phase resetting in the system. Modulating this ratio could switch periodic activity in a network on or off, and it is plausible that biological networks may avail themselves of this switching mechanism.

Implications for CPG design

Previously, in the same pyloric neurons, responses to excitatory inputs have been shown to be noisier than their responses to inhibitory inputs for both model and

biological neurons (Elson et al. 1999; Selverston et al. 2000). Although we have not taken the excitatory and inhibitory measurements in the same biological neuron, these differences likely exist and are due to the intrinsic properties of the neurons in question, rather than to experimental error. The lowered reliability in the production of predictable phase locked activity may explain why most CPGs rely predominantly on inhibition.

Excitatory synapses are not entirely absent from all CPGs, but they do not dominate. For example, although it has been shown that patterned activity in the lamprey hemicord is supported by a population of excitatory neurons without any inhibition, the full system appears to be dominated by inhibition, because coordination of left-right activity in the segmental half center oscillators is lost when inhibition is blocked (Cangiano and Grillner 2005). In salamander (Cheng et al. 1998) and mammalian spinal cord (McCrea and Rybak 2008), synchronized activity of flexor and extensor motor neurons has been observed in reciprocally coupled excitatory networks when inhibitory synaptic transmission was blocked. However, biologically relevant CPG coordination was again found to rely on one or several levels of half center oscillators that organize alternating flexor-extensor motor neuron activation.

The large number of special cases we found (20% of all networks) imply that excitatory synapses are not well suited to implement 1:1 phase-locking. This may help explain why we see few excitatory synapses utilized in biological CPGs. Well-studied CPGs such as those in the pyloric and gastric networks of the STG, leech heartbeat, and mollusk feeding are coupled with exclusively inhibitory synapses. Our results provide two reasons why networks coupled by excitation are less suitable to carry on rhythmic, phase-locked firing than those coupled by inhibition. First, networks with excitatory, but

not inhibitory, connections can be unstable due to positive feedback as in the case of runaway excitation. To maintain stability in an excitatory network, synapse strengths must be carefully constrained with respect to the noise level, resulting in increased regulatory load on the biological system. Second, discontinuities in the PRCs of component neurons of excitatory-coupled networks illustrate a mechanism whereby noise can cause modes of phase-locking to appear or disappear. In sum, the examination of phase resetting and its contribution to phase locking in excitatory compared to inhibitory networks provides an explanation of why inhibition generally predominates in central pattern generators, but also suggests that excitatory networks could be advantageous in contexts in which only brief, transient synchronization is required, as in the communication-through-coherence hypothesis (Fries 2005).

CHAPTER 3: INCLUSION OF NOISE IN ITERATED FIRING TIME MAPS BASED ON THE PHASE RESPONSE CURVE

At the time of writing, this chapter is in press (Sieling et al. 2010).

Introduction

The infinitesimal phase response curve (PRC) of a neural oscillator to a weak input is a powerful predictor of network dynamics; however, many networks have strong coupling and require direct measurement of the PRC for strong inputs under the assumption of pulsatile coupling. We incorporate measured noise levels in firing time maps constructed from PRCs to predict phase-locked modes of activity, phase difference, and locking strength in 78 heterogeneous hybrid networks of 2 neurons constructed using the dynamic clamp. We show that noise may either destroy or stabilize a phase-locked mode of activity.

The problem of synchronization and patterning of synchronization of oscillators is a problem that is of general interest in physics (Hansel et al. 1993; Golomb and Rinzel 1994; Izhikevich 1998; Dhamala et al. 2004; Fischer et al. 2006; Velazquez et al. 2007). More specifically, the study of pulse-coupled oscillators has commanded substantial interest (Goldsztein and Strogatz 1995; Foss et al. 1996; Gerstner 1996; Ernst et al. 1998; Goel and Ermentrout 2002; Timme et al. 2002; Earl and Strogatz 2003; Talathi et al. 2009). Networks of pulse-coupled oscillators are used to study many things (Winfree 2001)- e.g., plate tectonics (Olami et al. 1992), heart rhythms (Jalife 1984), and neural networks (Gerstner 1995). Synchrony is a dynamical feature of such networks (Mirollo and Strogatz 1990; Ernst et al. 1995; Bressloff et al. 1997). These systems consist of

oscillators coupled by discrete pulses. Phase response theory is often used to study network synchrony. The phase response curve (PRC) is tabulated as the shift in phase of an oscillator in response to a stereotyped input pulse (Glass and Mackey 1988). When the pulse is sufficiently weak, interactions can be added linearly so the infinitesimal PRC (iPRC), or response to weak perturbations, which is the foundation for a powerful technique—the theory of weakly coupled oscillators—can be used to predict network activity (Ermentrout and Chow 2002), however, many real systems are coupled too strongly for weak coupling approaches (Oprisan and Canavier 2001; Oprisan et al. 2004).

Phase response theory has a rich history in biological oscillators- especially in cardiac electrophysiology and neurophysiology. In the latter field, phenomena emerging from networks of two neurons are often used to help understand behaviors of networks containing large populations of neurons (Gerstner 1995), however, this paradigm is limiting - the complexity seen in biology is far beyond that explained by existing models, which are largely limited to networks of identical neurons coupled identically and weakly with no noise included. Conversely, real neural systems often contain heterogeneous neural types coupled heterogeneously, strongly, and with noise. Several recent studies have pushed one or more these boundaries, e.g. showing noise-stabilized antiphase oscillations (Ermentrout and Saunders 2006), synchronization in a network despite noise (Bendels and Leibold 2007), optimal PRC shape for noise-driven synchrony (stochastic synchrony) (Abouzeid and Ermentrout 2009), and bistability induced by shared noise (Ly and Ermentrout 2009). Although noise has been included in maps of pulse-coupled neurons (Netoff et al. 2005) , no study has yet formalized the effects of noise in non-

55

weakly coupled pulse-coupled networks. In (Sieling et al. 2009) we briefly proposed a method to address these issues simultaneously, and we applied it in one example as a proof of concept.

Here, we present our method formally and apply it generally to describe 78 experimental networks from (Sieling et al. 2009). We explicitly incorporate noise measured during experimental determination of the PRC into the prediction method. In a hybrid network of two bursting neural oscillators coupled via synaptic excitation ($\tau_{syn} \approx 10ms$ with a network period of about a second), we found that this method could accurately predict phase locking in the presence of 10% variability in the intrinsic period. We have shown that networks including a biological oscillator may undergo noise-induced transitions, and that including measured noise in the firing time map may capture the effect of noise, giving results that are qualitatively and quantitatively similar to experiment (Sieling et al. 2009).

Methods

Adding noise directly into the PRC

Following the biological tradition (Glass and Winfree 1984; Reyes and Fetz 1993), in a two neuron network our phase response curves (PRCs, F_{qi} below) describe the effect of a stereotyped input from the partner neuron j on neuron i as a function of the timing of input, or phase ϕ_i. The qth order PRC is tabulated experimentally

$$F_{qi}(\phi_i) = (P_{0i} - P_{qi})/P_{0i}$$

by measuring the qth cycle lengths P_{qi} and P_{0i}, where first order resetting q=1 measures response in the perturbed cycle, and second order resetting q=2 measures response in the next subsequent cycle. As such, F_{1i} measures the change of the cycle containing the start of input from neuron j

$$F_{1i}(\phi_i) = (P_{0i} - P_{1i})/P_{0i}.$$

If the input is an infinitesimal voltage deflection, then our F_{1i} is equivalent to PRCs used in weak coupling theory (Ermentrout and Kopell 1991; Hansel et al. 1995). Second order resetting F_{2i} has been previously shown to be important in bursting neurons (Oprisan and Canavier 2001; Oprisan et al. 2004; Sieling et al. 2009) and was recently modeled as leftover charge in dendrites resulting in partial reset (Kirst et al. 2009).

We use these PRCs to construct a general model of pulse-coupled phase oscillators with no delays

$$\dot{\phi}_i = \frac{1}{P_{0i}} + \sum_j F_{1i}(\phi_i)\delta(t - t_j^*), \tag{2}$$

where $\phi_i \in [0,1)$ is the phase of neuron i modulo 1. A threshold event such as a spike or burst occurs when the phase reaches one, and the phase is immediately reset to zero afterwards. The coupling function is given by F_{1i}, δ is the Dirac delta function, and t_j^* is the time of a spike or burst initiation in neuron j. Because we use ideas from phase resetting theory, we constrain the behavior of our uncoupled oscillators to autonomous periodic activity, i.e., spiking or bursting, where for each neuron i there is an intrinsic

period P_{0i} such that $\phi_i(t+P_{0i})=\phi_i(t)$. Note that the oscillators may be heterogeneous, each having its own intrinsic period $P_{0i} \neq P_{0j}$.

The major drawback to using PRCs as coupling functions in our model is that we must assume the system returns to its limit cycle between pulses. In the phase space this means that when a relatively strong input moves the coupled oscillator far from its uncoupled trajectory, it must return before the next input arrives. In general, this is not a problem for weakly coupled oscillators. Returning to the limit cycle between inputs also implies that in the case of a neuron receiving multiple inputs in between two firing events, the second order effects F_{2i} must be zero for all inputs except the last one received before the 2$^{\text{nd}}$ event. For two neurons, this is rarely a problem.

To expand (2) for non-weak inputs, we include F_{2i} by adding a second term, where ϕ_i^{last} is the value of ϕ_i at the last t_j^* if an input was received by neuron i in the previous cycle.

$$\dot{\phi}_i = \frac{1}{P_{0i}} - \sum_j F_{1i}(\phi_i)\delta(t-t_j^*) - A_i F_{2i}(\phi_i^{\text{last}})\delta(t-t_i^*)$$
$$\phi_i \geq 1: A_i \to 0 \qquad\qquad (3)$$
$$\phi_j \geq 1: A_i \to 1$$

The switch A_i is one if an input was received in the previous cycle and zero otherwise. Additionally, each ϕ_i must now be defined for small negative values because if F_{2i} is a delay, ϕ_i will be reset to a negative value. A geometrical interpretation of the negative branch in ϕ_i is given in (Oh and Matveev 2009) − it "corresponds to an isochron that curls around the limit cycle, intersecting it at a position that is retrograde to the peak of the action potential." For $\phi_i < 0$, F_{qi} are undefined, however, this is not a problem in our

analysis, where we assume that for $\phi_i < 0$, $F_{qi}(\phi_i) = F_{qi}(0)$ because few inputs (if any) were received on this branch.

To account for noise in our experimentally measured PRC data, we simply include it directly in the PRCs,

$$F_{1i}(\phi_i) = F_{1i}^{fit}(\phi_i) + \xi_{1i}\sigma_{1i}(\phi_i),$$

$$F_{2i}(\phi_i) = F_{2i}^{fit}(\phi_i) + \xi_{2i}\sigma_{2i}(\phi_i), \tag{4}$$

where F_{qi}^{fit} is a piecewise polynomial fit to the experimental data, ξ_{qi} represents unitary Gaussian noise, and σ_{qi} is the standard deviation of the measured noise as a function of ϕ_i, found by binning the data and measuring in each bin. All PRCs used in this study are the same as in (Sieling et al. 2009).

Consider a network of two heterogeneous coupled neural oscillators as in (3). To find modes of rhythmic network activity, we modify the iterative pulse coupled map with no predetermined firing order from (Achuthan and Canavier 2009) to include noise in the PRCs as in (4). We iterate the map as follows, where $\varphi_i[m]$ is the phase of neuron i after all effects of the previous pulse event m are added, S[m] is the set of neurons that emit a pulse m, and R[m] is the set that receives a pulse.

We initialize each neuron with a phase $\varphi_i[0]$ and a memory of second order resetting $F_{2i}(\varphi_i^{last}[0])$. Then, we poll for which neuron(s) will fire next: if $P_{0i}(1 - \varphi_i[m]) = \min\{P_{0i}(1 - \varphi_i[m])\}$ over all i, then $i \in S[m]$, else $i \notin S[m]$. If i sends a pulse then j receives one: for $i \in S[m]$, $j \in R[m]$ else $j \notin R[m]$, where $i \neq j$. Now update each neuron according to whether it fires a pulse and whether it receives a pulse: If $i \in S[m]$, $i \notin R[m]$, then reset φ_i to zero plus F_{2i} from previous cycle: $\varphi_i[m+1] = 0 - A_i F_{2i}(\varphi_i^{last}[m])$,

and reset the switch A_i to zero. If $i \in S[m]$, $i \in R[m]$, then set $\varphi_i[m+1] = 0 - A_i F_{2i}(\varphi_i^{last}[m])$ - $F_{1i}(\varphi_i[m] + (t[m+1] - t[m])/ P_{0i})$, and reset the switch A_i to zero. . If $i \notin S[m]$, $i \in R[m]$, then advance phase by elapsed time plus 1st order resetting from current cycle: $\varphi_i[m+1] = \varphi_i[m] + (t[m+1]-t[m])/P_{0i} - F_{1i}(\varphi_i[m]+(t[m+1]-t[m])/P_{0i})$. Update the memory of 2nd order resetting: for $i \in R[m]$, $\varphi_i^{last}[m+1]=\varphi_i[m] + (t[m+1] - t[m])/ P_{0i}$, and set the switch A_i to one. Now start again - poll for which neuron(s) will fire next, etc. To summarize:

For $i \in S[m]$, $i \notin R[m]$, $\varphi_i[m+1]= 0 - A_i F_{2i} (\varphi_i^{last}[m])$, $A_i =0$

For $i \in S[m]$, $i \in R[m]$, $\varphi_i[m+1] = 0 - A_i F_{2i}(\varphi_i^{last}[m])$ - $F_{1i}(\varphi_i[m] + (t[m+1] - t[m])/ P_{0i})$, $A_i =0$

For $i \notin S[m]$, $i \in R[m]$, $\varphi_i[m+1] = \varphi_i[m] + (t[m+1]-t[m])/P_{0i} - F_{1i}(\varphi_i[m]+(t[m+1]-t[m])/P_{0i})$, $\varphi_i^{last}[m+1]=\varphi_i[m] + (t[m+1] - t[m])/ P_{0i}$, $A_i =1$

This map is difficult to analyze because of the discontinuities introduced by the min function. First, there is no assumption of firing order. It is even possible that the neurons will fire synchronously or that one neuron will not fire at all. Next, a neuron's phase is updated differently depending on whether it fires a pulse, receives a pulse, or does both simultaneously. Note that the phase is updated each time that an input is received, in contrast to the weak coupling assumption where phase is not updated when each pulse is received based on resetting that occurs earlier in the cycle.

We have ignored conduction delays here, although they may be added to the map (Woodman and Canavier 2009). In our experimental system consisting of bursting neurons, we defined an event as the start of a burst in the presynaptic neuron. Using the

map, we can iterate a number of cycles N_{map} roughly matching the number of observed cycles N_{obs} and compare results using circular statistics as in (Sieling et al. 2009). The inclusion of noise in the firing time map is similar to (Netoff et al. 2005); the major difference is the use of F_2 in addition to F_1 in our method. Further, we explicitly restrict the tails of ξ_i according to their causal limits. In (Sieling et al. 2009), these limits translate to recovery interval tr≥0 and stimulus interval ts≥0 as defined below.

Results

Comparison of map to experimental data and noise-free method
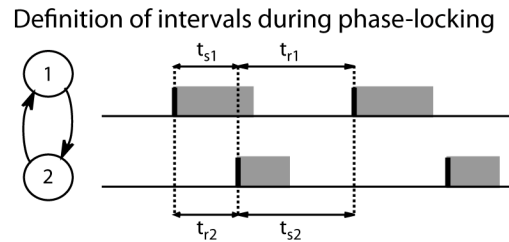
Figure 12. Definition of terms, A: stimulus time (ts) and response time (tr) during 1:1 phase locking are shown for bursting neurons 1 and 2. The shaded regions correspond to the burst duration, which can be a substantial fraction of the cycle period.

To evaluate our methods on experimental networks, we applied them to an existing dataset of 78 coupled networks (Sieling et al. 2009). These networks are constructed from one biological neuron and one model neuron by using the dynamic clamp (Sharp et al. 1993; Prinz et al. 2004) to implement artificial synapses. The biological neuron used (N=5) was the AB/PD complex from the pyloric network in the Stomatogastric ganglion of *Homarus Americanus*, which is a regularly bursting group of 3 electrically coupled neurons that act as a single oscillator. This group was isolated pharmacologically using standard methods (Sieling et al. 2009). The model neurons used

were from a heterogeneous set of four regularly bursting pyloric model neurons from a database (Prinz et al. 2003).

We compared experimental observations to predictions made using a noise-free method of pulsatile coupling (Oprisan et al. 2004; Sieling et al. 2009) and to the predictions of our iterated map using steady state stimulus intervals ts for each neuron in the network, where ts is the interval between the time of an event in one neuron and the time of the next input it receives from its partner neuron (Figure 12). For the case of 1:1 locking this is equivalent to t[M] above, where M is the set of odd or even whole numbers. Using both methods, we predicted qualitative behavior — whether a mode of 1:1 phase-locking would be observed — and quantitative behavior — the stable phase difference and strength of phase-locking. We quantify the strength of phase-locking using the circular statistic R^2. When each n of N phase differences $\Phi[n]=2\pi*ts_1[n]/P_{net} \in$ [0, 1), $P_{net}=\dfrac{1}{N}\sum_{n=1}^{N}(ts_1[n]+ts_2[n])$ is plotted on the unit circle, then $R^2 \in [0,1]$ is the length of the vector from the origin to the average position of the plotted points (Drew and Doucet 1991; Gutkin et al. 2005). We used a threshold $R^2 > 0.7$ to define phase-locking as in (Sieling et al. 2009).

In the 78 networks tested, the noise-free method was qualitatively incorrect 16 times and the iterative map was able to make the correct prediction for 8 of those networks (see (Sieling et al. 2009) for full analysis of the noise-free method in these networks) as well as 61 that were correctly predicted by the noise-free methods, for a total success rate of 69 out of 78, an improvement of 10%. We excluded eight networks that exhibited continuous spiking due to positive excitatory feedback as a result of the coupling, breaking the assumption of a limit cycle burster under which the PRCs were

generated (Sieling et al. 2009). Five failures of the map were due to overestimation of noise. Over the course of hours, noise levels in the biological neuron varied. In all cases, removing noise from the firing time map by setting $\sigma=0$ in (4) produced a match to the predictions of the noise-free method.
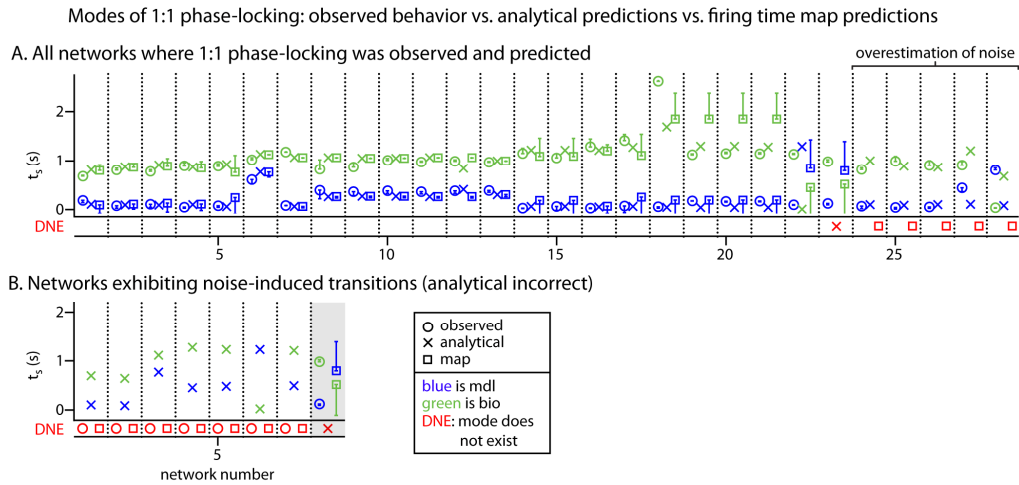
Figure 13. Map with noise. Comparison of observed behavior from (Sieling et al. 2009) to analytical and firing time map predictions including F_2 in the firing time map. Empirical observation (o and error bars), analytical prediction (x), and prediction using the firing time map (square and error bars) are shown for mdl (model neuron, blue) and bio (biological neuron, green) neurons in each hybrid network, separated by dotted lines and sorted by qualitative match for clarity. Modes that were not observed or predicted to exist are marked by a red symbol (o, x, or square) in the row labeled DNE. For clarity, error bars are shown only in one direction. Analytical predictions are noise-free so they do not have error bars. The x axis is the arbitrary experimental network number. A. For networks observed to phase-lock, the noisy map produced results that were generally in agreement with observations. In one case (red x) the noisy map succeeded where the noise free method failed, but in five cases (red squares) the noisy map failed presumably due to overestimation of noise. (B) In cases where noise was previously shown to cause the analytical prediction to fail, the noisy map correctly predicted the failure to lock in seven cases, and the noise-induced ability to lock, albeit with some error, in one case.

To best compare predictions made using our firing time map to those made using the noise-free methods, we focus on networks that were experimentally observed to phase-lock. In Figure 13, we compare methods for 28 such networks by showing steady state ts intervals for each neuron in the network. Each network is represented by an ordered group of symbols separated by vertical dotted lines, showing ts values obtained for each of the methods used. Where a phase-locked mode was not observed or predicted by a method, the appropriate symbol is plotted in red below.

64

When F_2 was removed from the firing time map (not shown), $F_{2i}=0$ in (3), prediction accuracy dropped from 85% to 45%, as we would expect from (Oprisan and Canavier 2001; Oprisan et al. 2004; Sieling et al. 2009). In B, we compare prediction methods in 8 networks previously shown to exhibit noise-induced transitions (Sieling et al. 2009). The analytical method, which is noise-free, was qualitatively incorrect in each of these cases, and the map was correct in each case. Out of the 8 networks with such behavior, only 1 was observed to phase-lock and the map method was qualitatively accurate (network 8, shaded). Note that in this network, the analytical methods did not predict a phase-locked mode, so adding noise to the PRCs caused a new stable fixed point to appear, showing that in the firing time map, *noise can both generate and destroy modes of phase-locking*.

Discussion

We have verified that variability in a PRC does modulate the strength of phase-locking in a network of 2 neurons. When noise was added to the map, the differential effects of noise on structurally stable and unstable systems was captured qualitatively and quantitatively using circular statistics. This simple idea is a powerful tool for understanding the predictive utility of PRCs because it simulates the measured variability of the biological neuron and gives outputs that are readily compared to experimental data.

Noise threshold and phase-dependency of noise

Bendels and Leibold (Bendels and Leibold 2007) note a threshold in noise level above which "low-synchrony" phase-locking occurs but is not predicted by their mean-field approximation method due to occasional slipping. This threshold can be explained

65

by the noise level at which the envelope of phase-dependent noise around the PRC disrupts the basin of attraction of the noise-free fixed point. We do not analyze this threshold here, but our data give examples where a stable fixed point in the noise-free system transitions to a quasi-stable fixed point when noise is added, seen as stable phase-locking with occasional slipping.

Accurate measurement of variability near a non-linear event

An input can never advance the event time to a time before the input was applied: this is the causal limit. If no input is given at phase ϕ, then the next event is expected to follow at a time interval of $P_0(1-\phi)$, the remaining interval. Therefore the observed phase resetting can never drop below the line ($F_{1i}(\phi)=\phi-1$), which biases the noise observed in first order PRCs. For example, in Tsubo et al. (Tsubo et al. 2007) the authors note that they could fit the distributions of the fluctuations in the phase responses at phases less than 0.5 with Gaussian distributions with a variance that was nearly constant. However, at phases greater than 0.5, the variance decreased. Fig. 2E of that paper makes it clear that the causal limit is responsible, but the role of the causal limit was not addressed. Phoka et al. show that noise in Purkinje cells introduces a bias in the mean measured PRC due to the causal limit (Phoka et al. 2008). To correct for the bias, they use all spikes in a train as reference, one at a time, rather than using only the spike before and after. Polhamus et al. proposed a different solution, which was to average only ISIs longer than the stimulus interval to determine the average period to use to calculate the phase. Our method accounts for the missing variance in the first order resetting by treating second order resetting separately.

Netoff et al. (Netoff et al. 2005) also observed PRCs in which the noise was limited by causality. In their studies of excitatory inputs, the scatter decreased inversely proportional to the square root of the phase, but for inhibitory inputs causality is not an issue and variance was independent of phase. Netoff et al. (Netoff et al. 2005) also incorporated noise into a PRC-based map. They chose firing times for each cell by adding the spike time response curve (STRC) value (mean + normally distributed random component scaled by the time-dependent SD, each measured from the STRC) to the unperturbed firing period of the cell in question (Netoff et al. 2005).

Since our map is different from that of Netoff et al. (Netoff et al. 2005) only in that that we used second order resetting, it is interesting that our maps perform more poorly if F_2 is ignored. This is likely because the neurons in (Netoff et al. 2005) are spiking, rather than the bursting neurons that we used, and spiking neurons tend to have small F_2 amplitudes. The new method incorporates the true variance rather than underestimating it at late phases. To our knowledge, this point has not been made previously. For example, after commenting on the phase dependence of the variance observed by Netoff et al., Ermentrout and Sanders state that "An adequate theory of this dependence remains to be resolved" (Ermentrout and Saunders 2006). In our method, the variance in F_2 in the subsequent cycle compensates for reduction in variance at late phases in F_1 .

CHAPTER 4: ARTIFICIAL RECONFIGURATION OF A REWARD-LEARNING NETWORK REVEALS CELLULAR MECHANISMS CAUSING TRANSITIONS IN A MOTIVATED BEHAVIOR

Introduction

Operant conditioning, which was introduced by (Thorndike 1911), is an example of associative learning in which an association is established between a specific behavior (the operant) and a stimulus (the reinforcement). A key feature of operant conditioning is the contingency of the reinforcement (i.e., the correlation between the expression of a designated operant behavior and the delivery of a reinforcement; (Skinner 1938; Konorski 1948)). As a result of this contingency the frequency of the reinforced behavior is modified. This phenomenon, known as the "law of effect" (Thorndike 1933), provided evidence that the nervous system has mechanisms by which a particular motor output can be selected from among many different behaviors that may be expressed.

Operant conditioning in the mollusk *Aplysia*'s food-seeking behavior produces a long-lasting switch from irregular, impulsive-like radula biting movements into stereotyped, compulsive-like recurrences of this cyclic act (Susswein et al. 1986). Experimentally, this change is induced by giving the reward, a splash of seaweed juice pipetted into the *Aplysia*'s mouth, after each occurance of the operant, a bite. After 1 hour of such treatment, the animal bites more frequently and more rhythmically.

An *in vitro* analog of this behavioral switch exists, where fictive motor activity is monitored in peripheral nerves while intracellular electrophysiology is done (Nargeot et al. 1997). Three bilateral pairs of initiating neurons (INs; B63, B65, and B30) in the

feeding central pattern generator (CPG) circuit found in the buccal ganglia (B.g.) are initiators of each radula bite motor pattern (BMP). In Figure 14, see that the INs reside bilaterally in the B.g. and are just one component of the feeding CPG.

Nargeot et al. (Nargeot et al. 2007; Nargeot et al. 2009), measured correlates of behavioral plasticity found in INs of the B.g. Naïve animals were trained as described above, then immediately dissected and tested *in vitro*. In this way, Nargeot et al. discovered changes in cellular properties that helped to clarify a possible mechanism underlying the behavioral changes induced during training. Among other things, they measured changes in the bursting properties of pattern-initiating neurons and increases in electrical coupling between individual neurons. Their dataset provided plausible correlates that might describe mechanisms of control, however, there was no way to follow the chain of causality in that data. Under the behavioral training paradigm, many aspects of the CPG could be changed, and there is no way to insure that the essential changes were measured. Using dynamic clamp methods, we were able to control specific cellular parameters to cause changes in fictive activity and thus tease apart the mechanism.

The dynamic clamp method (Sharp et al. 1993) allows the addition or subtraction of any voltage dependent conductance in the vicinity of the intracellular electrode. Given an electrotonically compact neuron and 4 IC electrodes, we were able to reconfigure the connectivity of 4 impaled neurons using a computer and detailed models. In this fashion, we discovered that the changes in electrical coupling and excitability measured by Nargeot et al. (2009) are sufficient to cause all changes in fictive behavior seen in the study. In naïve arrhythmic networks we show that increasing the electrical coupling

between pattern-initiating neurons caused burst length and rhythm regularization, correct (ingestive) motor pattern selection, and correct firing order (B63 leading) as compared to the behaviorally trained animals from Nargeot et al. (2009). Interestingly, we did not see any change in bite frequency.

Since our results on rhythm modulation were so convincing, we hypothesized that there may be a separate mechanism controlling rate. One such mechanism could be a leak conductance. Upon further testing, we found that leak did control rate and had no effect on rhythm. Here, we present the results that show for the first time that rhythm and rate are controlled independently and that adjustment of these basic network parameters in 3 or 4 out of the 6 relevant cells leads to a transition in fictive behavioral output. Further, these transformations are immediate, formally causal, and reversible.
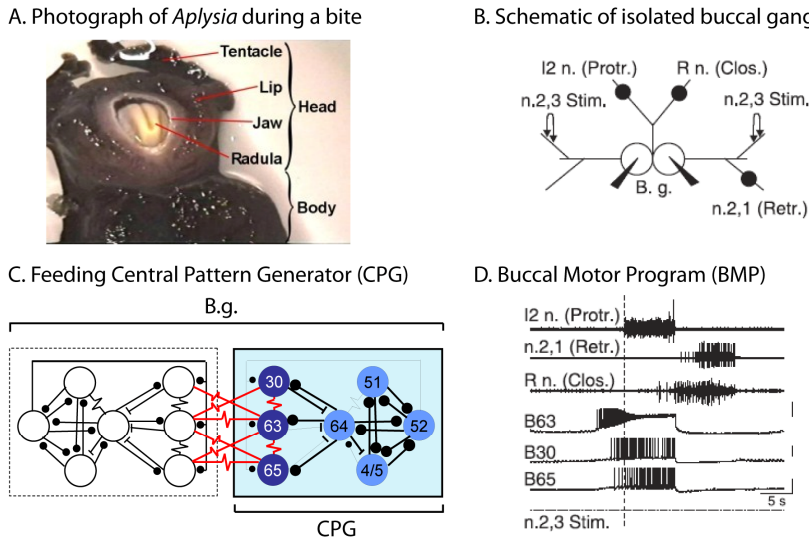
A. Photograph of *Aplysia* during a bite

B. Schematic of isolated buccal ganglia (B.g.)

C. Feeding Central Pattern Generator (CPG)

D. Buccal Motor Program (BMP)

Figure 14. Introduction to the buccal ganglion (B.g.) of *Aplysia*. (A) Photograph of the head and mouth of *Aplysia* during a bite. (**http://www.scholarpedia.org/article/Image:Mouth.jpg**) (B) Schematic of isolated bilateral B.g. showing placements of extracellular recording electrodes (filled circles) on the intrinsic muscle 2 motor nerve (I2 n.; radula protractor motoneurons), radula nerve (R n.; closure motoneurons), and nerve 2,1 (n.2,1; retractor motoneurons) and intracellular electrodes (arrowheads) for intrasomatic recordings. Bipolar stimulating electrodes (twin arrows) placed on the left and right 2,3 sensory nerves (n.2,3) were used to activate buccal feeding circuitry. (C) Schematic of the Feeding CPG in the B.g. Each ganglion may act as an independent CPG, so we show detail for only one side. Electrical couplings of interest to us are shown in red. (D) Simultaneous extracellular recordings of a single radula motor pattern (fictive bite) consisting of protractor (I2 n.), retractor (n.2,1), and closure (R n.) motoneuron bursts and intracellular recordings of the bilaterally paired B63, B30, and B65 pattern-initiating neurons during low-frequency inciting stimulation (2 Hz, 8.5V) of nerve n.2,3 (n.2,3 Stim.; horizontal dotted line). Note that the onsets of bursting activity in B63, B30, and B65 preceded the initial protraction phase (indicated by the vertical dashed line) of the fictive bite. Vertical scales represent 20 mV.

Methods

Animals

Adult *A. fasciata*, which are found locally from August to November in the Bassin d'Arcachon (France), were supplied by the Lycée de la Mer (Gujan Mestras) and the Laboratoire de Biologie Marine (Arcachon). *A. californica* were purchased from the University of Miami (Fl, USA) and were used in the seasonal period when local A. fasciata are unavailable. Animals were maintained at 15°C in filtered artificial sea water

71

(ASW) until used, and were fed daily with fresh seaweed (Ulva lactuca) obtained from the Lycée de la Mer and the Station de Biologie Marine at Roscoff (France). The animals remained unfed for 2 days before experiments to stimulate food-seeking during food-reward training.

Electrophysiology

Adult *Aplysia fasciata* and *Aplysia californica* were used in experiments, which in agreement with a previous study (Katzoff et al. 2002) revealed no interspecies differences in behavioral or electrophysiological characteristics. The appetitive operant training protocols used were as described in detail previously (Nargeot et al. 2007).

Animals were anesthetized by the injection of 50-100 ml of $MgCl_2$ into their hemolymph. After isolation, the bilaterally-paired buccal ganglia (B.g.) were pinned out in a Sylgard-lined Petri dish containing ASW (mM): NaCl, 450; KCl, 10; $MgCl_2(6H_2O)$, 30; $MgSO_4$, 20; $CaCl_2(2H_2O)$, 10; Hepes, 10 (pH adjusted to 7.4 with HCl). The preparations were maintained at 15°C by means of a Peltier cooling device and were not superfused during the actual experiment.

Extracellular recordings and stimulations were made using wire electrodes placed against selected peripheral nerves (Figure 14B). Monopolar (recording) and bipolar (stimulation) electrodes were insulated from the bath with Vaseline petroleum jelly. Radula motor patterns, each consisting of motor nerve bursts that would normally drive protraction, retraction and closure phases of a radula bite cycle, were elicited by monotonic stimulation (8.5 V, 0.3 ms at 2 Hz) of the two bilateral 2,3 nerves (n.2,3) generated by a single Grass S88 stimulator and delivered through a photo-isolation unit.

Intracellular recordings and stimulations were made from de-sheathed ganglia with glass microelectrodes (tip resistance ~10-20 MΩ) filled with 2 M KCH3CO2. All recorded signals were amplified by Axoclamp-2B amplifiers (Molecular Devices, Palo Alto, CA), visualized on a Tektronix 5113 oscilloscope, digitized by an analog to digital converter (CED 1401, Cambridge Electronic Design, UK) and analyzed with Spike2 software (Cambridge Electronic Design, UK).

Intrasomatically-recorded B30, B63 and B65 neurons were identified electrophysiologically according to the following criteria: Firstly, they produce spontaneous bursting activity that occurs during the protraction phase of each radula motor pattern. Second, they have no axonal projections in peripheral buccal nerves, and third, they all produce mixed chemical excitatory and electrotonic synaptic potentials in the contralateral B31/32 motoneurons. Moreover, B30 has no axonal projection in the cerebro-buccal connectives (CBC), it produces IPSPs and a long-lasting activation of the bilateral B8 motoneurons and it does not make conventional synaptic connections with the B61/62 motoneurons. B63 was identified on the basis of its axonal projection in the contralateral CBC, a unique excitatory synapse with the contralateral B61/62 motoneurons and its lack of a conventional synapse with B8. B65 was identified by its absence of axonal projections in the CBCs and its production of facilitating EPSPs in the bilateral B61/62 motoneurons.

The strength of electrical coupling between selected pairs of neurons was calculated as the ratio of the maximum postsynaptic voltage response to the corresponding maximum presynaptic voltage deflection elicited by a 2 s negative current pulse. In these experiments, two presynaptic electrodes were again used, one to maintain

the cell's resting membrane potential at - 70 mV and for additional negative current pulse injection, while the other electrode was used for voltage recording. The resting membrane potential of the postsynaptic neuron, which was simultaneously impaled with a third electrode, was not altered experimentally during the recording of the electrical synaptic potential.

Dynamic clamp methods

We used dynamic clamp methods (Sharp et al. 1993; Prinz et al. 2004) to add artificial membrane conductances to real neurons. We used 3 different types of artificial conductances. Each was a voltage dependent conductance. To calculate the current that would flow through such a conductance if it were present, the membrane potential V_m was recorded and routed to either a dedicated microprocessor (CED 1401 below) or a standard desktop computer (RTXI below). At an update timestep between 100 and 1000 μs (1 to 10 kHz, noted below), V_m was used to calculate the momentary current, and a command signal was routed to the current clamp amplifier, which delivered current until the next timestep.

Electrical coupling between neurons

To deliver artificial electrical coupling between 2 neurons, we wrote a dynamic clamp protocol to continuously measure V_m for each neuron and calculate the current using Ohm's Law $I_{ec}=G_{ec}*(V_{m1}-V_{m2})$, where current $i_1=-I_{ec}$ is the current injected into cell 1 and $i_2=I_{ec}$. For networks with more than 2 neurons, the current injected into each neuron was calculated as the sum of currents at each cell according to Kirchoff's Current Law.

<u>Leak conductance</u>

Leak conductance G_{leak} was added by assuming a leak reversal potential E_{leak} near the cell's resting membrane potential V_{rest}, where $I_{leak}=G_{leak}*(V_m-E_{leak})$. Our choice of E_{leak} was tailored to each individual cell so that G_{leak} would not affect V_{rest}. To do this, we set E_{leak} as close to V_{rest} as possible without going above. In INs of the B.g., V_{rest} varies by cell type and by animal, so we allowed E_{leak} to also vary appropriately. This choice of E_{leak} follows previous work (Zhao et al. 2010).

<u>H-type conductance</u>

H-type conductance Gh are not well studied in B.g. neurons, so in this study we adapted a well-know Gh from another invertebrate system, the Pyloric network of the Stomatogastric Nervous System (originally from guinea pig), where

$$I_h = G_h m_\infty (V_m - E_h),$$

$$m_\infty = \frac{1}{1 + \exp\left(\dfrac{V - V_{th}}{5.5}\right)},$$

$$\tau_m \frac{dm}{dt} = (m_\infty - m),$$

$$\tau_m = \frac{2}{\exp(\dfrac{V + 169.7}{-11.6}) + \exp(\dfrac{V - 26.7}{14.3})},$$

E_h=-50 mV, and V_{th}=-75 mV (Huguenard and McCormick 1992; Prinz et al. 2003). The differences we note between the Pyloric network and the feeding network of the B.g. are in frequency (1 s vs. 30 s, respectively) and plateau potentials (these vary by cell type in

both systems). To adjust for these differences, we chose Eh=-25 mV and Vth=-25 mV, and we scaled τ_m by a factor of 30 to slow it down.

Positive and negative conductances

For each conductance we added using the dynamic clamp, we were also able to subtract that conductance by setting the relevant G value to a negative number. This negative conductance should be interpreted as canceling out the effect of an existing membrane process, such as a population of ion channels, on V_m. While adding a conductance is straight-forward, subtracting is less so because there is no biological analog to a negative ion channel. For this reason, we took precautions when subtracting conductances not to subtract a larger G value that we expected to exist.

CED1401

Some of our experiments were done using custom software written in a proprietary Assembly-like language controlling a microprocessor on the CED1401plus (Cambridge Electronic Design, UK; (Sieling 2009)) that can store and run a limited number of user-defined instructions at precise timesteps. We used this system to run preliminary experiments for electrical coupling of 3 and 4 cells. Update timestep was limited to 1 ms, however, this was sufficient to observe spikes coupled across Gec.

About the CED1401 microprocessor

The CED1401 series DAQ boards are built to interface with CED's Spike2 software suite, which contains a proprietary scripting language and is popular among electrophysiologists. Beyond A/D and D/A conversion, the CED1401 has an onboard

microprocessor—called the "sequencer"—that supports up to 1023 Assembly-like instructions, which can be uploaded to its memory. The microprocessor can generate precisely timed digital pulses and analogue voltages and respond to input data in real time. The microprocessor clock runs at a constant, user-defined rate of up to 100 instructions per millisecond. It controls the 1401 DACs (Digital to Analogue Converters), can read the latest value from a waveform channel, supports loops, and has 64 variables that can be read and set by on-line scripts. Using this information, real-time (fractions of a millisecond) responses to input data changes are possible (CED manual).

RTXI

Some of our experiments were done using custom software written in C++ to interact with the Real-Time eXperiment Interface (www.rtxi.org) and a NI PCI-6259 data acquisition card (National Instruments). All experiments using G_{leak} and G_h were done using this system. While we were able to use update frequencies up to 20 kHz (50 μs) using RTXI, we had better results with a slower rate. Extracellular stimulation artifacts (stimulation parameters were 8.5 V, 0.3 ms at 2 Hz; see *Electrophysiology*) were consistently observed as high frequency ringing on one or several microelectrodes. At high update frequencies, these artifacts were also observed by the dynamic clamp program, causing inappropriate currents to be injected. To prevent this, we chose a slower update frequency 3 kHz which removed most stimulation artifacts from our V_m signals by virtue of the Nyquist sampling theorem. At this rate, we were still able to observe spikes injected due to G_{ec}. Aliasing of the stimulation artifacts was not a problem.

About RTXI

RTXI is an open source real-time Linux based software system for hard real-time data acquisition and control applications. RTXI is a modified linux kernel that maintains hard real time performance by protecting the microprocessor from user interrupts. Because RTXI uses the microprocessor of a modern personal computer rather than a small dedicated microprocessor, it allows for shorter update intervals and greater flexibility compared to the CED1401 system described above.

In our use, RTXI interfaces with the Axon amplifiers via a DAQ board connected to a PCI slot of the computer. To input (output) a signal, RTXI must tell the DAQ to perform ADC (DAC), and then the analog input (output) signals are sent to system memory (the amplifiers). RTXI must control ADC and DAC function, so open source drivers are needed for any DAQ to be used with RTXI. There are were no open source CED DAQ drivers available at the time of our experimental setup, so we could not use the CED1401 DAQ device with RTXI. Once we had obtained interesting data using the CED1401 system, we purchased an M-series NI DAQ board with 4 analog inputs and outputs and set it up with an RTXI system.

Data Analysis

The regularity of radula motor patterns or neuronal impulse burst occurrences was assessed by autocorrelation analysis as described previously (Nargeot et al. 2007). Nonparametric statistical procedures were used for both paired and independent data group comparisons, which were subjected where appropriate to post hoc significance testing. Differences were considered significant when $p < 0.05$.

To assess the temporal organization of fictive radula bite cycles or of spike bursts in individual neurons, autocorrelations were computed by Spike2 software over a fixed number of successive events: either 100 radula motor patterns recorded extracellularly from motor nerves, 800 action potentials in intracellular recordings of B30 and B65 neurons, or 2000 action potentials in intracellular recordings from B63 neurons. The differences in numbers of analyzed events in the different cell types reflected their typical spontaneous firing frequencies. Autocorrelations were then expressed as histograms of 2.5 s bin widths over ranges of 150 s or 300 s for the analysis of extracellularly-recorded motor patterns and intracellularly-recorded action potentials, respectively. The choice of these time scales reflected the slower burst frequencies of individual neurons in response to depolarizing current injection as compared to the shorter cycle periods of motor patterns generated by the buccal network under tonic stimulation of the peripheral 2,3 nerve.

Buccal ganglion activity was considered as rhythmically recurrent when the corresponding autocorrelation histogram could be fitted (correlation coefficient r_0 at a significant level of $p\_0.05$) by a damped sinusoidal Gabor function (Engel et al. 1990; Young et al. 1992) according to

$$y(x) = y_0 + \left[a \sin\left(\frac{2\pi}{b} x + c \right) \right] \times \exp\left(-\frac{x^2}{2d} \right),$$

with parameters of amplitude (a), period (b), initial phase lag (c) and time constant (d)$\neq 0$ at $p \leq 0.05$, an amplitude of at least 10% above offset ($a/y_0 > 0.1$), and a minimum of three peaks $\sqrt{d/b} > 0.8$ (Young et al. 1992). In some cases, we were unable to obtain 100 radula motor patterns, but the Gabor fit was still significant. In these cases,

79

we used the data only when the Gabor significance had changed between experimental conditions. Computations of these parameters, fitting data by nonlinear regression, and testing of statistical significance of the parameters and of the correlation coefficient (*r*) were performed with Sigma Plot software (Systat, Richmond, CA).

Results

To test whether cellular changes correlated to contingent-reward training are necessary and sufficient for observed changes in behavior—increased rhythmicity and rate—we used the dynamic clamp to control one or several membrane conductances in the *in vitro* analog of operant conditioning (Nargeot et al. 1997). We tested the effects of electrical coupling G_{ec} between INs and changes in G_{leak} and G_h in individual INs. We were able to test both criteria using naïve starved preparations, which may exhibit either type of behavior, e.g. we could add G_{ec} to a non-rhythmic preparation to test if it is sufficient to change the behavior, then in a contingent preparation we could subtract G_{ec} to test if that property is necessary for the changed behavior. Naïve preparations behave differently—80% display non-contingent (non-rhythmic) and 20% display contingent (rhythmic) fictive behavior—so we were able to test both populations without using the laborious behavioral training protocols described in Nargeot et al. (Nargeot et al. 1997), however, the preponderance of our data come from preparations of the non-contingent type. This work was done entirely in the lab of John Simmers in Bordeaux, France during 3 summer-time trips. At the time of writing, we are not able to present statistical group comparisons in every figure. These comparisons are forthcoming, but they are not presented here.

Electrical coupling affects rhythm but not rate

In naïve nonrhythmic networks, BMPs occurred irregularly under free-running conditions. When electrical coupling was turned on, bursts in INs and BMPs showed a stable rhythm. We show a representative example in Figure 15, where many features of the *in vitro* analog of operant conditioning are evident. When coupling is turned on: 1) the fictive behavior seen in the extracellular recordings show rhythmic ingestion patterns, 2) neuron 63 leads all BMPs, 3) burst lengths in intracellular recordings are regularized. Gabor function fits show rhythm regularization (Figure 15B). Electrical coupling had no measurable effect on BMP frequency (Figure 15C). In rhythmic preps, we set G_{ec} = -15 nS to remove the effect of existing electrical coupling on the network. This operation was the opposite of that shown in Figure 15, and we observed the opposite effect- an immediate change from rhythmic to arrhythmic activity (not shown). We measured changes in burst length variability in naïve nonrythmic preps. Using the same bursts used for Gabor fits, we measured coefficient of variation (σ/μ, where σ is standard deviation and μ is mean) for the 2 groups—with and without electrical coupling— and found that burst lengths were less variable with the coupling turned on (Figure 15D). Likewise, we measured a decrease in burst dispersion or an increase in the regularity of phase differences between INs (not shown).
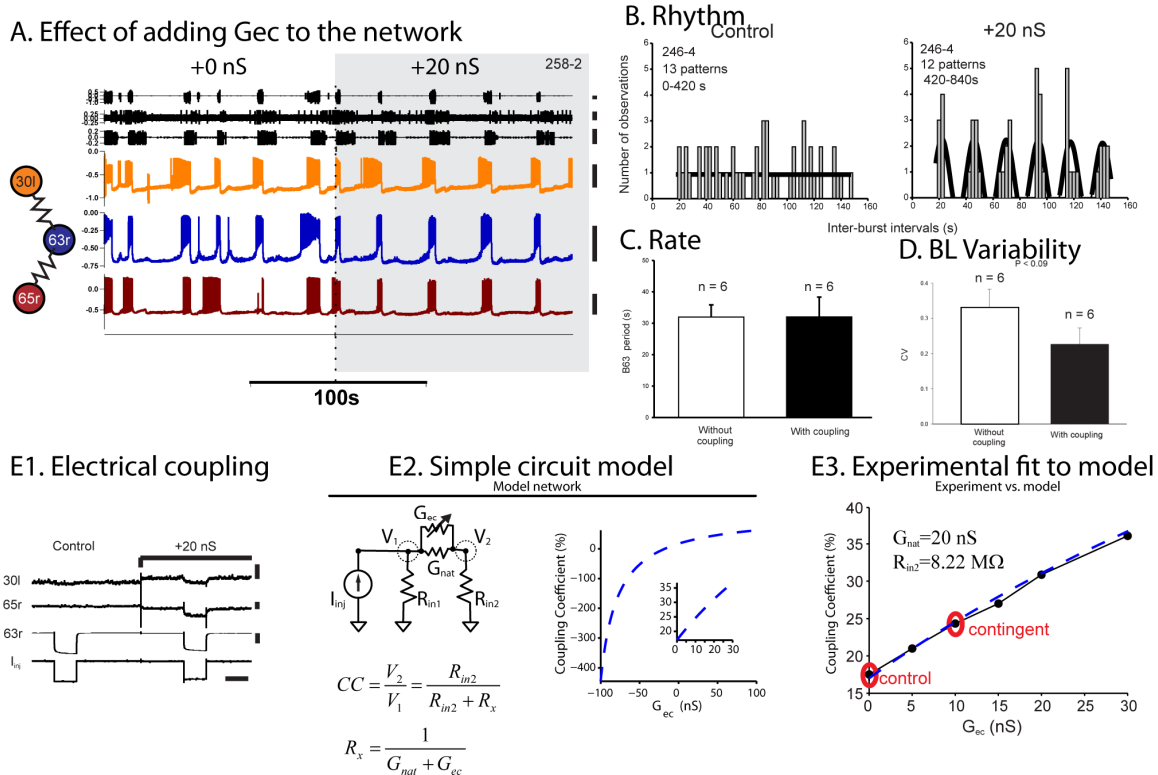
Figure 15. Effects of G_{ec} on naïve arrhythmic network. (A) Fictive motor activity immediately changes when G_{ec} is applied. From top to bottom, traces are: extracellular recordings from peripheral nerves I2 n. (protr.), n.2.1 (Retr.), R n. (Clos.), intrasomatic recordings from B30, B63, B65 (scale bars at right are 50 mV). (B) Histograms of BMP activity (grey boxes) with Gabor function fits (thick black lines) showing change in rhythmicity. (C) Group comparison showing no significant (n.s.) change in BMP rate due to G_{ec} (N=6). (D) Group comparison showing reduced burst length variability due to G_{ec} (N=6, p<0.05). (E) Effect of artificial electrical coupling on measured coupling coefficient. From left to right: (E1) current injected into B63 has no effect on B65 or B30 until G_{ec} is turned on (+20 nS), (E2) in a simplified circuit model of electrical coupling we show the effect of G_{ec} on coupling coefficient (V2/V1), given the natural electrical coupling G_{nat} and the input impedances R_{in}, (E3) comparison of model and experimental data (Rin1=Rin2=8MΩ). Red circles indicate where G_{ec} caused the measured coupling coefficient to equal the control (ctrl) or contingent values measured in Nargeot et al. (2009).

To check that we used an appropriate strength of electrical coupling, we measured a dose-response curve for G_{ec} vs. Coupling Coefficient (CC) (Figure 15E3). For the cells shown, we found that G_{ec}=10 nS was sufficient to increase CC to contingent levels. This value varies from cell to cell and given that we inject current at the soma while gap

junctions are located in the neuropil, it is reasonable to use 20 nS as recently described in another invertebrate system (Zhao et al. 2010).

From a simple electrical model, we can see that this curve is non-linear, but in the range that we measured experimentally, it should appear linear (Figure 15E2). By hand, we fit values for G_{nat} and R_{in2} to match the y-intercept (Gec=0) and slope of experimental data (E3). We see the critical value (CC=0) where we should limit our use of negative G_{ec} values (E2; near -20 nS, given G_{nat}=20 nS). For the given model, this is where G_{ec}<0 has completely counteracted the native electrical coupling G_{nat} and stronger G_{ec} has no biological significance. This value is not sensitive to changes in R_{in2} on the scale of changes previously reported, between 4 and 7 MΩ (Nargeot et al. 2009).

Isolated configurations

To test whether the effect of G_{ec} was CPG-dependent or only IN-dependent, we conducted the same experiment while functionally isolating the INs from the CPG (Figure 16). By hyperpolarizing one B63 neuron, the CPG is silenced. Using the amplifier's voltage offset control, the hyperpolarized B63 neuron (63r) was adjusted back to its resting potential and coupled to 63l. At this time, we depolarized 63l, initiating bursting activity. We also depolarized 65r and coupled it to the bursting 63l. We found that in this configuration, the effect of G_{ec} was the same as when the CPG was functional—that is—the effect is that G_{ec} causes a marked and immediate increase in rhythmicity.
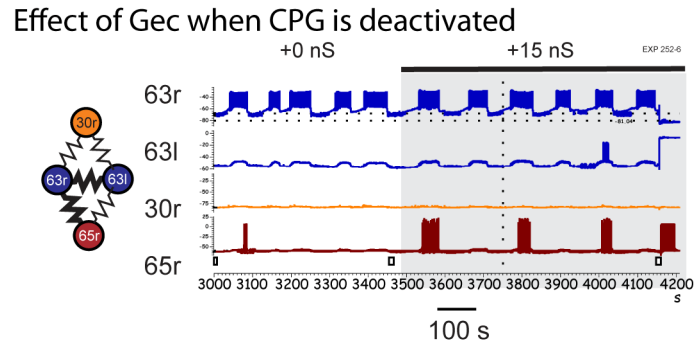
Figure 16. Effect of G_{ec} when CPG is deactivated. Scale bars are 50 mV.

<u>B64 is not necessary for increased rhythmicity</u>

B64 is a member of the feeding CPG, but it is not an IN. B64 is a retraction neuron with strong ipsilateral inhibitory projections onto all INs (Figure 14). Due to this type of connectivity, B64 could act to synchronize the INs, however, we show that B64 is not necessary for increased rhythmicity. In Figure 16, B63l was hyperpolarized, thus the CPG was not active and B64 was never activated. This is confirmed extracellularly by the absence of retraction motor activity, yet electrical coupling still induced regular bursting.

Leak conductance affects rate but not rhythm

In arrhythmic preps, artificial leak conductances G_{leak} subtracted from INs immediately caused increased BMP frequency with no effect on rhythm (Figure 17). In rhythmic preps, we found the inverse was true—leak added to the INs immediately caused decreased BMP frequency with no effect on rhythm (not shown).
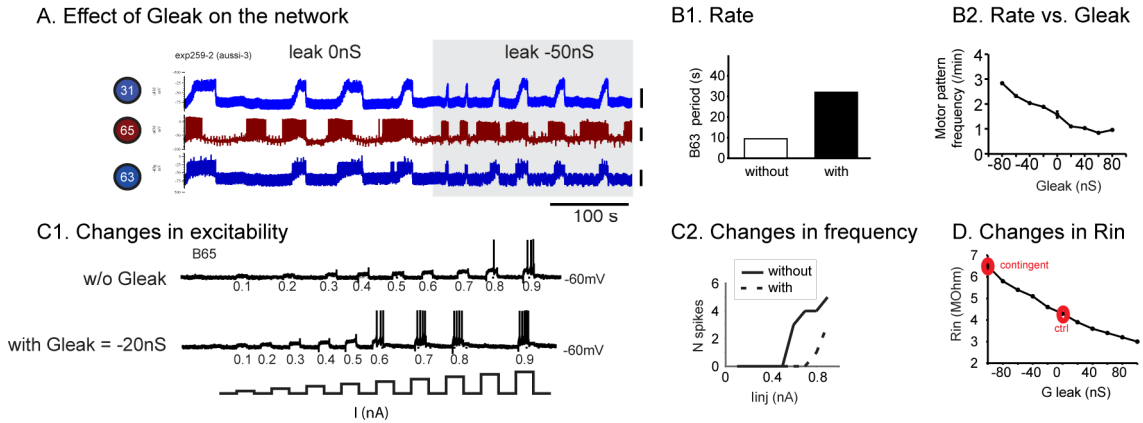
84

Figure 17. Effect of G_{leak} on network. (A, B1) As in **Figure 15**. (A) Scale bars are 50 mV. (B1) Rate vs. G_{leak} as G_{leak} is varied (N=10 BMPs per measurement). (C1) Excitability protocol. (C2) Spike frequency. (D) Rin as a function of G_{leak}. Red circles indicate where G_{leak} caused measured Rin to equal the control (ctrl) or contingent values measured in Nargeot et al. (2009).

To check that G_{leak} was affecting IN excitability, we tested this directly (Figure 17D). To control for resting membrane potential (V_{rest}) variation, we injected current to bias the cell to a fixed V_{rest}, then measured spike threshold and spike frequency by injecting I_{inj} in (0.0,1.0) nA in steps of 0.1 nA. In all preps, G_{leak} increased spike threshold and decreased spike frequency (and vice versa for negative G_{leak}).

Further, we measured changes in input impedance (R_{in}) due to I_{leak} (Figure 17E). This relationship is non-linear as expected from calculating the equivalent resistance for a constant R_{in} (MΩ) and variable G_{leak} (nS) added in parallel $R_{eq}=1/(\ 1/R_{in} + G_{leak}/1000)$. For the preparation shown, G_{leak}=-100 nS gives the R_{in} measured in contingent preps (red circle; Nargeot et al. 2009), so we take this as a reasonable value to use for our dynamic clamp experiments. These measurements were taken in two-electrode current clamp mode.

Electrical coupling plus leak conductance switches network from non-contingent to contingent fictive motor behavior

To test for the compatibility of G_{ec} and G_{leak} mechanisms, we applied them simultaneously to non-rhythmic preparations (Figure 18). Our results are simply the combination of each individual experiment- indicating that the 2 mechanisms may not interact, rather they act independently. As seen in the above sections, where either G_{ec} or G_{leak} was applied, we see the same results here- increased rate and rhythm. This effect was not sensitive to small changes in G_{ec} or G_{leak}. Additionally, we applied this method in reverse. We trained animals as previously described, by contingently pipetting seaweed juice into the intact animal's mouth cavity, then performed experiments *in vitro*. In Figure 19, we show that adding $-G_{ec}$ and $+G_{leak}$ recover the fictive behavior of an untrained animal, irregular BMPs at a reduced rate.

Non-contingent: In untrained animals

A1. Gec
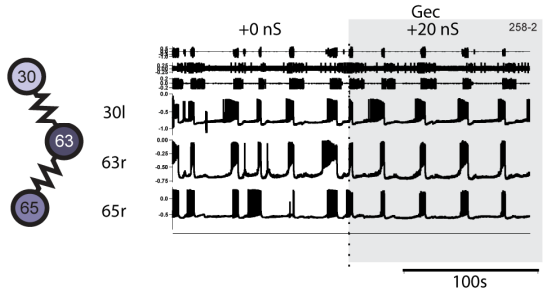
A2. Rhythm
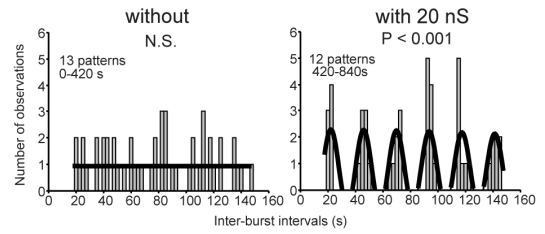
B. Gleak
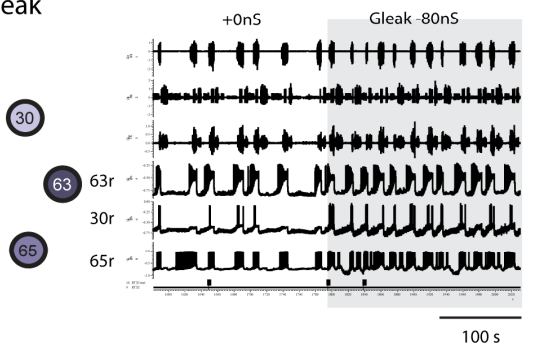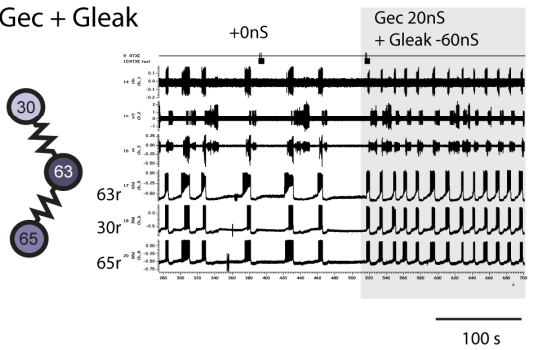

C1. Gec + Gleak

C2. Rhythm

Figure 18. G_{ec} plus G_{leak} are manipulated in untrained animals to reproduce fictive behavior seen in trained animals. All panels are as described in **Figure 15**. Scale bars are 50 mV.

Contingent: In trained animals

A. Gec

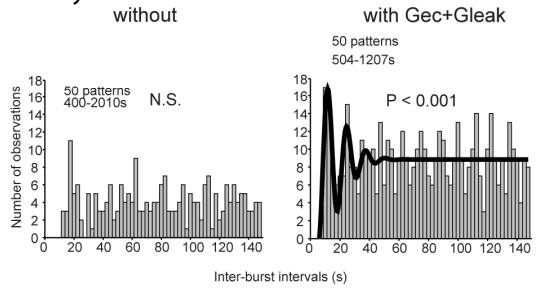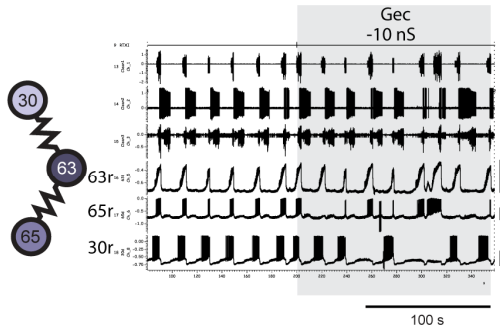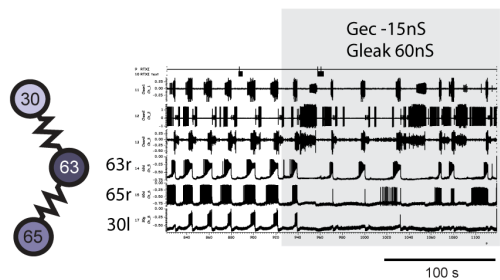### B1. Gec + Gleak

B2. Rhythm
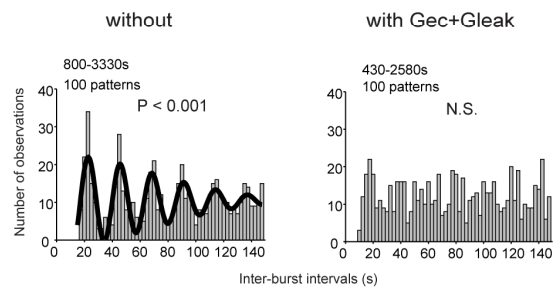
Figure 19. G_{ec} plus G_{leak} are manipulated in trained animals to recover fictive behavior seen in untrained animals. All panels are as described in **Figure 15**. Scale bars are 50 mV.

Coupling does not affect V_{rest} or network period

In all measured groups, V_{rest} and network period was similar. No significant differences were found in the initial resting membrane potentials of recorded postsynaptic neurons in the different experimental groups of preparations (Figure 20), indicating that changes in the coupling coefficient between cell pairs in the different experimental groups were not due to initial differences in postsynaptic membrane potential. The bi-directionality of coupling between cells was also verified qualitatively by injecting current via the single post-junctional recording electrode and recording the voltage response in the previously pre-junctional neuron. There was also no change in V_{rest} when G_{leak} was modified by dynamic clamp (not shown).

88
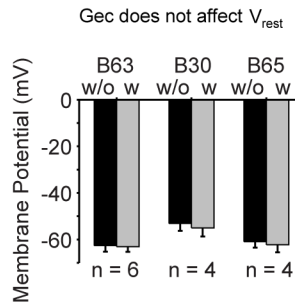
Figure 20. Group comparisons for each IN type showing no change in V_{rest} after adding G_{ec}.

Discussion

We have built on the work of others to elucidate mechanisms underlying operant conditioning in a behaviorally relevant motor pattern generating network. Previous work described correlates of operant conditioning that were dependent on Dopamine (Nargeot et al. 2007; Nargeot et al. 2008; Nargeot et al. 2009). Neuromodulators like Dopamine can have many effects (Harris-Warrick et al. 1998), so it was impossible to know which effects were important. In this work, we make quantifiable changes that clearly link cause and effect, giving reversible results that explain how the interaction of 2 cellular mechanisms underlie operant conditioning. More generally, we describe basic mechanisms of interest for future learning and memory research. Regulation of gap junctions is currently a major area of interest (Perez Velazquez and Carlen 2000; Perez Velazquez et al. 2001; Christie et al. 2005; Migliore et al. 2005; Kokarovtseva et al. 2009), however, to our knowledge they have never before been so directly implicated in learning.

How does electrical coupling regularize BMP generation?

Electrical coupling G_{ec} can have different effects depending on the cellular characteristics of the coupled neurons (Perez Velazquez et al. 2001). To our knowledge, G_{ec} has been implicated in increasing burst period (Sherman and Rinzel 1992), changing spiking to bursting (Komendantov and Canavier 2002), regulation of burst duration (Abbott et al. 1991), increasing dynamic range of oscillation (Soto-Trevino et al. 2005), synchronization (Galarreta et al. 2004; Migliore et al. 2005), normal motor behavior in rats (Moore and Grace 2002), and learning in rats (Kokarovtseva et al. 2009). While it's beyond the scope of this paper to distill the dynamical features of INs that support our reported observations, we can speculate that the addition of G_{ec} in naïve arrhythmic networks causes a transition in the phase portrait of the network of INs, generating a new stable orbit or stabilizing an existing unstable one. Below, we detail the effects of G_{ec} to inform any future models.

Using our dynamic clamp systems, individual spikes generated in one cell caused voltage deflections in the partner cell that looked like attenuated spikes. Also, plateau potentials in one cell caused steady current to be passed to the partner cell. In Figure 16, we saw rhythmic activity in B63r while B63l was silent, so steady currents may be more important, but at this point we don't know if the fast interaction of spikes or slow interaction of plateau potentials is more important for the observed regularization of activity.

Because we coupled different cell types, V_{rest} varied from cell to cell, resulting in a small constant current passed between cells. It's important to note that each interaction between two cells causes an equal amount of current to be passed into one cell as is

90

removed from its partner. From the view of charge, these interactions are equal and opposite, however, these are real neurons, which are heterogeneous in many aspects including input impedence R_{in}, so it's possible that one cell could have a net excitatory effect on the other without experiencing significant inhibition. We have observed this effect in both directions, but have not conducted an analysis.

Different configurations

In several network configurations, we saw similar increases in rhythmicity (not shown). After surveying several of the 510 possible different configurations of 2 to 4 INs, we choose 2 configurations for further study based on theoretical and empirical data. The first configuration consists of 4 cells: B63-B63-B65-B30. This configuration includes both pacemakers B63 and one each of the other 2 IN cell types, one from each side. The second configuration consists of 3 ipsilateral cells: B63-B65-B30. We have not done a deep survey, but our experience is that it is of primary importance to couple all different IN cell types and secondary to couple both B63 pacemaker cells. We have replicated our major findings with most configurations of 2, 3, and 4 cells that we have tried. We measured changes in rhythmicity and rate in several conformations. Our experience is that the effect of G_{ec} is increased when (a) the B63 neurons are coupled, and (b) when more INs are coupled. We tested couplings of 2 INs, including coupling the 2 B63 neurons, and we found a mild effect. This is why we present G_{ec} data from experiments where we coupled 3-4 neurons. As a control, we coupled 4 CPG neurons that were not INs: B31/32r and B31/32l. We saw no effect, so we expect that this is not a population

phenomenon. The effect of G_{ec} on burst regularity was stronger ipsilaterally by coupling different cell types 30/63/65 rather than contralateral pairs of the same cells.
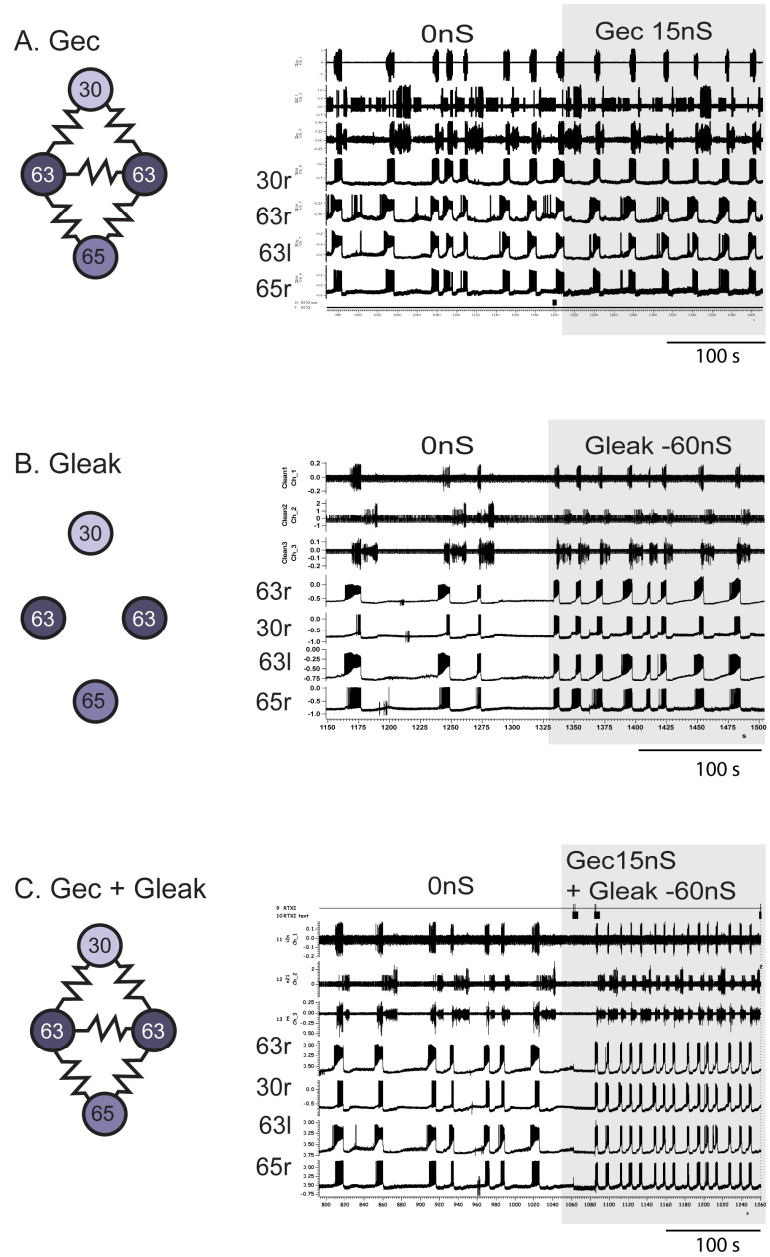

Figure 21. Effects of G_{ec} and G_{leak} in the 4 cell configuration. All traces are as in **Figure 15**. Scale bars are 50 mV.

How does G$_{leak}$ increase frequency?

As described in some detail in Zhou et al. (2010), the effect of a +G$_{leak}$ is to add or strengthen an attracting stable fixed point at V$_m$=E$_{leak}$ (+G$_{leak}$ represents the addition of leak, -G$_{leak}$ subtraction). Likewise, the effect of –G$_{leak}$ is to add a repelling unstable fixed point at E$_{leak}$. For a strong magnitude of -G$_{leak}$ this can cause the cell to be bimodal, where it is either hyperpolarized, remaining below E$_{leak}$ as enforced by the strength of –G$_{leak}$, or depolarized, remaining above E$_{leak}$. Experimentally, we can choose E$_{leak}$ slightly below V$_{rest}$ to push the cell towards depolarization and increased excitability, however, this is likely to also change V$_{rest}$. Since our goal with –G$_{leak}$ was to reduce the effect of the endogenous leak channel population, and we expect this leak to be primarily a K+ dependent process, we choose E$_{leak}$ slightly below V$_{rest}$, often at V$_{rest}$-5 mV. This small offset had no measureable effect on V$_{rest}$ when compared to controls, but did alter the dynamics, sometimes significantly, where we could observe large swings in burst frequency as E$_{leak}$ was changed from slightly above V$_{rest}$ to slightly below or vice versa. Such sensitivity is to be expected—it comes from the dynamics of the system as described above and in the Zhou paper.

<u>H-type conductance affects rate—does it effect rhythm?</u>

Since many membrane mechanisms can affect excitability, we also tried adding a model of the H-type conductance (I$_h$). We saw increased rate but also sensitivity in V$_{rest}$. We were able to choose the parameters of I$_h$ such that V$_{rest}$ was not affected in one cell, but it was more difficult than for G$_{leak}$. We did not observe an effect on rhythm, although this is theoretically possible.

Control of firing order

We have observed that it is common to observe the correct firing order (B63, B30, B65) in naïve nonrhythmic networks after adding G_{ec} artificially, however, this is not always the case. Sometimes we observed rhythmic activity with inappropriate firing order. The simplest explanation that our data supports is that natural G_{leak} modulation is cell-type or activity dependent. This type of modulation is consistent with a previous description of Dopamine modulation in lobsters (Harris-Warrick et al. 1998). Our hypothesis is that G_{leak} decreases more in B63 than in other INs so that it is the most excitable and begins bursting first.

Dopamine dependency

The neurotransmitter, dopamine (DA), is commonly thought to play a critical role in motivated behaviors and their adaptations by learning. Nargeot et al. (Nargeot et al. 1999; Nargeot et al. 2008) tested the effects of exogenously-applied DA on the B.g. *in vitro* and found that it produces the same set of correlates to operant conditioning as measured previously- increased electrical coupling between INs and a change from arrhythmic to rhythmic activity in INs, however, it was unknown what other effects of DA might exist. In this work, we show that a limited group of cellular correlates is causal to the observed behavioral switch. While DA has been previously implicated in many modulatory roles, e.g. (Harris-Warrick et al. 1998), it seems that in the B.g., one important role is in the regulation of G_{ec} and G_{leak}, regardless of what other regulatory roles DA may occupy.

Biological significance

Of synchrony/rhythmicity for the animal?

The brain (or behavior) switches from an erratic trial/error state to a strongly motivated (compulsive) state. Our dynamic clamp experiments show that synchrony is necessary for rhythmicity- there is a causal relationship between synchrony and rhythmicity.

Of independent mechanisms for rhythm and rate control

We show that independent cellular mechanisms may control the rhythm and rate of the feeding CPG in the B.g. Now we should ask- what advantage does this confer? Is there a functional advantage for the animal? Is there a situation where the animal may prefer to ingest its food quickly and rhythmically or slowly and rhythmically? This could be an interesting direction for future investigation.

Synapse-mediated effects

We have not investigated any effects of synapse-mediated network reconfiguration. This work was motivated by Nargeot et al. (2009), and they did not report any such changes. While we work with identified neurons in the B.g., the full feeding network has not been described. The INs we study receive many post-synaptic potentials (PSPs) from unidentified neurons, however, these synapses are not of primary importance as far as we know.

Buccal ganglion modeling

Single compartment models that include Hodgkin-Huxley ion channels that roughly reproduce B.g. neuron activity exist (Baxter et al. 1999; Susswein et al. 2002), however, the ion channels present in B63, B65, and B30 have not been studied in depth. No model of the feeding CPG exists. To our knowledge, it is not known for each neuronal type which channels are present or what are the conductance densities of these channels. We think that it will be important in the future to obtain voltage clamp data characterizing these channels. Further, there is much to be discovered about intracellular processes that may contribute to the intermittent bursting seen in naïve arrhythmic preparations, such as Calcium dynamics.

CHAPTER 5: CONCLUSIONS

Neuroscience and ultimately psychology aims to describe the activity of frighteningly complex neural networks. To accomplish this requires research input from many levels. Rhythmic activity has been found important at many levels, from single pancreatic beta cells to spatially disparate ensembles of cortical neurons supporting facial recognition. Pathological rhythms such as those found in Parkinson's and epilepsy have put a human face on the importance of understanding how such rhythms work and fail.

We focused on small networks consisting of identified neurons that have known connections. We aimed to understand the rhythmic properties of these networks at the cell membrane, where a rich literature of experimental and theoretical work already exists. Our ultimate goal is to develop basic theory that can scale up to large heterogeneous networks. This will impact not only medicine but also may provide insight into biological function of information processing, which could be applied algorithmically.

Our methods include electrophysiology, theory of coupled non-linear oscillators, and dynamic clamp. First, we evaluated a theory of pulse-coupled oscillators for networks of 2 bursting neurons coupled via excitation. Then, we extended this theory to include the effects of natural biological variability. Finally, we described a novel mechanism for a network to switch from irregular to rhythmic activity.

Aim 1- Chapter 2

In Chapter 2, we validated existing pulsatile coupling methods for networks of 2 neurons coupled by artificial chemical synaptic excitation in networks consisting of one

biological and one model neuron. These networks were heterogeneous in terms of synaptic strength, burst length, and intrinsic period. We used a well studied biological neuron with several common bursting mechanisms—plateau potentials, frequency adaptation, and post-inhibitory rebound—so that our results apply to a wide range of neurons. We found that the methods were generally good, accurately predicting our observations of phase-locking for most networks, including those that phase-locking via a depolarization block mechanism; however, because we studied a large parameter set, we found 2 special cases in the data where it was necessary to extend the theory. The first special case was a common problem of feedback excitation (runaway excitation). In this case, recurrent excitation caused one or both neurons to change from rhythmic bursting to tonic spiking. This occurred when at least one synapse was strong. The second special case was due to a combination of the natural variability in intrinsic frequency and the structure of the excitatory PRC. PRCs in response to excitation are more complex than inhibitory ones. These may take several morphological forms, some of which include an apparent discontinuity. When the natural variability is large enough to push the system over this discontinuity, then we say that the phase-locked mode has been destroyed by noise. To investigate the effects of this noise, we created firing time maps that included noise in the PRCs, and we showed as a proof of concept that the noise levels we measured experimentally are capable of destroying phase-locking. In response to an ongoing curiosity—why all CPGs are dominated by inhibitory synapses rather than excitatory ones—we applied our new general knowledge of the rhythmic properties of excitatory synapses to conclude that they are less suitable for the robust rhythmic activity

that is the hallmark of a CPG. Rather excitation seems better suited for brief, transient synchronization.

Aim 2- Chapter 3

In Chapter 3, we made a formal description and systematic study of the firing time maps we created in Chapter 2. A significant motivation of this work was to communicate our findings effectively to a more technical audience that has recently begun to study problems of noise and heterogeneity in great depth. We verified over a large dataset that variability in a PRC does modulate the strength of phase-locking. We showed that noise may create or destroy phase-locked modes of activity. Additionally, we found that our maps help explain 1) a noise threshold at which phase-locking is broken, and 2) the phase-dependency of noise, especially near the causal limit. This work essentially added another tool that may be used in the present to explain the effects of noise and heterogeneity on experimental data and in the future to evaluate new theoretical concepts.

Aim 3- Chapter 4

In Chapter 4, we broke away from existing theoretical methods to study new mechanisms of rhythm generation in an important biological context. Using the dynamic clamp, which we used above to verify theory, we reconfigured part of the feeding CPG for the mollusk *Aplysia* to show exactly what mechanisms support learning in this network. Following correlative experimental data showing changes in coupling coefficients and excitability, we changed electrical coupling between neurons and leak conductance in single neurons. By applying these manipulations separately and together,

we showed that they are independent. Electrical coupling controls rhythm and leak controls rate. To our knowledge, these results make the feeding CPG the best understood reward-learning system to date.

Overall conclusions

In modern research, theoretical and experimental work is often executed separately. Different people in far-away places half-way around the Earth are working on the same problem. In our studies, we have simplified that process. This work includes experimental exploration and theoretical development. While it has been a pleasure to work in this flexible mode, it has also been a benefit to our work. Experimentally, we have been efficient, designing experiments that directly advise theory. Theoretically, we have enjoyed knowledge of the limits of experimental data, staying close to the data to avoid passing those limits. We have validated and extended a theory and dissected a mechanism that relates to rhythmic behavior of neural networks.

REFERENCES

Abbott, L. F. and Marder, E. (1999). Modeling small networks. Methods in neuronal modeling. C. Koch and I. Segev: 361-410.

Abbott, L. F., Marder, E. and Hooper, S. L. (1991). "Oscillating networks: Control of burst duration by electrically coupled neurons." Neural Comput. **3**(4): 487-497.

Abouzeid, A. and Ermentrout, B. (2009). "Type-ii phase resetting curve is optimal for stochastic synchrony." Physical Review E **80**(1).

Achuthan, S. and Canavier, C. (2008). "Phase response curves determine network activity of all to all networks of pulse coupled oscillators." BMC Neuroscience **9**(Suppl 1): P135.

Achuthan, S. and Canavier, C. C. (2009). "Phase-resetting curves determine synchronization, phase locking, and clustering in networks of neural oscillators." J Neurosci **29**(16): 5218-5233.

Arshavsky, Y. I., Deliagina, T. G., Orlovsky, G. N. and Panchin, Y. V. (1989). "Control of feeding movements in the pteropod mollusk, clione-limacina." Experimental Brain Research **78**(2): 387-397.

Arshavsky, Y. I., Grillner, S., Orlovsky, G. N. and Panchin, Y. V. (1991). Central generators and the spatiotemporal pattern of movements. The development of timing control and temporal organization in coordinated action: Invariant relative timing, rhythms, and coordination. J. Fagard and P. H. Wolff. Amsterdam, Elsevier: 93-115.

Baxter, D. A., Canavier, C. C., Clark, J. W., Jr. and Byrne, J. H. (1999). "Computational model of the serotonergic modulation of sensory neurons in aplysia." J Neurophysiol **82**(6): 2914-2935.

Bendels, M. H. K. and Leibold, C. (2007). "Generation of theta oscillations by weakly coupled neural oscillators in the presence of noise." Journal of Computational Neuroscience **22**(2): 173-189.

Benson, J. A. (1980). "Burst reset and frequency control of the neuronal oscillators in the cardiac ganglion of the crab, portunus-sanguinolentus." Journal of Experimental Biology **87**(AUG): 285-313.

Bressloff, P. C., Coombes, S. and deSouza, B. (1997). "Dynamics of a ring of pulse-coupled oscillators: Group theoretic approach." Physical Review Letters **79**(15): 2791-2794.

Calabrese, R. L. and Peterson, E. L. (1983). Neural control of heartbeat in the leech, *hirudo medicinalis*. Neural origin of rhythmic movements. A. Roberts and B. Roberts. Cambridge, UK, Cambridge Univ. Press: 195-221.

Canavier, C. C., Baxter, D. A., Clark, J. W. and Byrne, J. H. (1999). "Control of multistability in ring circuits of oscillators." Biol. Cybern. **80**: 87-102.

Canavier, C. C., Butera, R. J., Dror, R. O., Baxter, D. A., Clark, J. W. and Byrne, J. H. (1997). "Phase response characteristics of model neurons determine which patterns are expressed in a ring circuit model of gait generator." Biol. Cybern. **77**: 367-380.

Cangiano, L. and Grillner, S. (2005). "Mechanisms of rhythm generation in a spinal locomotor network deprived of crossed connections: The lamprey hemicord." Journal of Neuroscience **25**(4): 923-935.

Cheng, J., Stein, R. B., Jovanovic, K., Yoshida, K., Bennett, D. J. and Han, Y. (1998). "Identification, localization, and modulation of neural networks for walking in the mudpuppy (necturus maculatus) spinal cord." J. Neurosci. **18**(11): 4295-4304.

Christie, J. M., Bark, C., Hormuzdi, S. G., Helbig, I., Monyer, H. and Westbrook, G. L. (2005). "Connexin36 mediates spike synchrony in olfactory bulb glomeruli." Neuron **46**(5): 761-772.

Cui, J., Achuthan, S., Canavier, C. C. and Butera, R. J. (2008). Periodic vs. Transient estimation of phase response curves. APS March Meeting. New Orleans, LA.

Dayan, P. and Abbott, L. F. (2001). Theoretical neuroscience, MIT Press.

de la Iglesia, H. O., Cambras, T., Schwartz, W. J. and Diez-Noguera, A. (2004). "Forced desynchronization of dual circadian oscillators within the rat suprachiasmatic nucleus." Current Biology **14**(9): 796-800.

Dhamala, M., Jirsa, V. K. and Ding, M. Z. (2004). "Enhancement of neural synchrony by time delay." Physical Review Letters **92**(7).

Dorval, A. D., Christini, D. J. and White, J. A. (2001). "Real-time linux dynamic clamp: A fast and flexible way to construct virtual ion channels in living cells." Annals of Biomedical Engineering **29**(10): 897-907.

Drew, T. and Doucet, S. (1991). "Application of circular statistics to the study of neuronal discharge during locomotion." Journal of Neuroscience Methods **38**(2-3): 171-181.

Earl, M. G. and Strogatz, S. H. (2003). "Synchronization in oscillator networks with delayed coupling: A stability criterion." Physical Review E **67**(3).

Elson, R. C., Huerta, R., Abarbanel, H. D., Rabinovich, M. I. and Selverston, A. I. (1999). "Dynamic control of irregular bursting in an identified neuron of an oscillatory circuit." J Neurophysiol. **82**(1): 115-122.

Engel, A. K., Konig, P., Gray, C. M. and Singer, W. (1990). "Stimulus-dependent neuronal oscillations in cat visual cortex: Inter-columnar interaction as determined by cross-correlation analysis." Eur J Neurosci **2**(7): 588-606.

Ermentrout, B. and Saunders, D. (2006). "Phase resetting and coupling of noisy neural oscillators." J Comput Neurosci **20**(2): 179-190.

Ermentrout, G. B. and Chow, C. C. (2002). "Modeling neural oscillations." Physiol Behav **77**(4-5): 629-633.

Ermentrout, G. B. and Kopell, N. (1990). "Oscillator death in systems of coupled neural oscillators." SIAM Journal on Applied Mathematics **50**(1): 125-146.

Ermentrout, G. B. and Kopell, N. (1991). "Multiple pulse interactions and averaging in systems of coupled neural oscillators." Journal of Mathematical Biology **29**(3): 195-217.

Ermentrout, G. B. and Rinzel, J. (1984). "Beyond a pacemaker's entrainment limit: Phase walk-through." Am J Physiol Regul Integr Comp Physiol **246**(1): R102-106.

Ernst, U., Pawelzik, K. and Geisel, T. (1995). "Synchronization induced by temporal delays in pulse-coupled oscillators." Physical Review Letters **74**(9): 1570-1573.

Ernst, U., Pawelzik, K. and Geisel, T. (1998). "Delay-induced multistable synchronization of biological oscillators." Physical Review E **57**(2): 2150-2162.

Fell, J., Klaver, P., Lehnertz, K., Grunwald, T., Schaller, C., Elger, C. E. and Fernandez, G. (2001). "Human memory formation is accompanied by rhinal-hippocampal coupling and decoupling." Nature Neuroscience **4**(12): 1259-1264.

Fischer, I., Vicente, R., Buldu, J. M., Peil, M., Mirasso, C. R., Torrent, M. C. and Garcia-Ojalvo, J. (2006). "Zero-lag long-range synchronization via dynamical relaying." Physical Review Letters **97**(12).

Foss, J., Longtin, A., Mensour, B. and Milton, J. (1996). "Multistability and delayed recurrent loops." Physical Review Letters **76**(4): 708-711.

Fries, P. (2005). "A mechanism for cognitive dynamics: Neuronal communication through neuronal coherence." Trends in Cognitive Sciences **9**(10): 474-480.

Galarreta, M., Erdelyi, F., Szabo, G. and Hestrin, S. (2004). "Electrical coupling among irregular-spiking gabaergic interneurons expressing cannabinoid receptors." J Neurosci **24**(44): 9770-9778.

Gerstner, W. (1995). "Time structure of the activity in neural-network models." Physical Review E **51**(1): 738-758.

Gerstner, W. (1996). "Rapid phase locking in systems of pulse-coupled oscillators with delays." Physical Review Letters **76**(10): 1755-1758.

Glass, L. and Mackey, M. (1988). From clocks to chaos.

Glass, L. and Winfree, A. T. (1984). "Discontinuities in phase-resetting experiments." Am J Physiol **246**(2 Pt 2): R251-258.

Goel, P. and Ermentrout, B. (2002). "Synchrony, stability, and firing patterns in pulse-coupled oscillators." Physica D-Nonlinear Phenomena **163**(3-4): 191-216.

Goldsztein, G. and Strogatz, S. H. (1995). "Stability of synchronization in networks of digital phase-locked loops." International Journal of Bifurcation and Chaos **5**(4): 983-990.

Golomb, D. and Rinzel, J. (1994). "Clustering in globally coupled inhibitory neurons." Physica D-Nonlinear Phenomena **72**(3): 259-282.

Gurel Kazanci, F., Maran, S., Prinz, A. and Canavier, C. (2008). "Predicting n:1 locking in pulse coupled two-neuron networks using phase resetting theory." BMC Neuroscience **9**(Suppl 1): P136.

Gutkin, B. S., Ermentrout, G. B. and Reyes, A. D. (2005). "Phase-response curves give the responses of neurons to transient inputs." J Neurophysiol **94**(2): 1623-1635.

Hansel, D., Mato, G. and Meunier, C. (1993). "Clustering and slow switching in globally coupled phase oscillators." Physical Review E **48**(5): 3470-3477.

Hansel, D., Mato, G. and Meunier, C. (1995). "Synchrony in excitatory neural networks." Neural Computation **7**(2): 307-337.

Harris-Warrick, R. M., Johnson, B. R., Peck, J. H., Kloppenburg, P., Ayali, A. and Skarbinski, J. (1998). "Distributed effects of dopamine modulation in the crustacean pyloric network." Ann N Y Acad Sci **860**: 155-167.

Harris-Warrick, R. M., Marder, E., Selverston, A. I. and Moulins, M. (1992). Dynamic biological networks. The stomatogastric nervous system. Cambridge, MIT Press.

Hartline, D. K. (1979). "Pattern generation in the lobster (panulirus) stomatogastric ganglion .2. Pyloric network simulation." Biological Cybernetics **33**(4): 223-236.

Hartline, D. K. and Gassie, D. V. (1979). "Pattern generation in the lobster (panulirus) stomatogastric ganglion .1. Pyloric neuron kinetics and synaptic interactions." Biological Cybernetics **33**(4): 209-222.

Hooper, S. L. (2004). "Variation is the spice of life. Focus on "cycle-to-cycle variability of neuromuscular activity in aplysia feeding behavior"." J Neurophysiol **92**(1): 40-41.

Horn, C. C., Zhurov, Y., Orekhova, I. V., Proekt, A., Kupfermann, I., Weiss, K. R. and Brezina, V. (2004). "Cycle-to-cycle variability of neuromuscular activity in aplysia feeding behavior." J Neurophysiol **92**(1): 157-180.

Huguenard, J. R. and McCormick, D. A. (1992). "Simulation of the currents involved in rhythmic oscillations in thalamic relay neurons." J Neurophysiol **68**(4): 1373-1383.

Izhikevich, E. M. (1998). "Phase models with explicit time delays." Physical Review E **58**(1): 905-908.

Jalife, J. (1984). "Mutual entrainment and electrical coupling as mechanisms for synchronous firing of rabbit sino-atrial pace-maker cells." Journal of Physiology-London **356**(NOV): 221-243.

Katzoff, A., Ben-Gedalya, T. and Susswein, A. J. (2002). "Nitric oxide is necessary for multiple memory processes after learning that a food is inedible in aplysia." J Neurosci **22**(21): 9581-9594.

Kirst, C., Geisel, T. and Timme, M. (2009). "Sequential desynchronization in networks of spiking neurons with partial reset." Physical Review Letters **102**(6): 068101-068104.

Kokarovtseva, L., Jaciw-Zurakiwsky, T., Mendizabal Arbocco, R., Frantseva, M. V. and Perez Velazquez, J. L. (2009). "Excitability and gap junction-mediated mechanisms in nucleus accumbens regulate self-stimulation reward in rats." Neuroscience **159**(4): 1257-1263.

Komendantov, A. O. and Canavier, C. C. (2002). "Electrical coupling between model midbrain dopamine neurons: Effects on firing pattern and synchrony." J Neurophysiol **87**(3): 1526-1541.

Konorski, J. (1948). Conditioned reflexes and neuronal organization. Cambridge, UK, Cambridge UP.

Luo, C., Canavier, C. C., Baxter, D. A., Byrne, J. H. and Clark, J. W. (2004). "Multimodal behavior in a four neuron ring circuit: Modes switching." IEEE Trans. Biomed. Eng. **51**: 205-218.

Ly, C. and Ermentrout, G. B. (2009). "Synchronization dynamics of two coupled neural oscillators receiving shared and unshared noisy stimuli." Journal of Computational Neuroscience **26**(3): 425-443.

Mancilla, J. G., Lewis, T. J., Pinto, D. J., Rinzel, J. and Connors, B. W. (2007). "Synchronization of electrically coupled pairs of inhibitory interneurons in neocortex." Journal of Neuroscience **27**(8): 2058-2073.

Maran, S. K. and Canavier, C. C. (2008). "Using phase resetting to predict 1 : 1 and 2 : 2 locking in two neuron networks in which firing order is not always preserved." Journal of Computational Neuroscience **24**(1): 37-55.

Maran, S. K., Sieling, F. H., Demla, K., Prinz, A. A. and Canavier, C. C. (2010). "Complex phase resetting of bursting neurons in response to excitation implies slow outward current and spatial segregation of burst generating mechanism." In preparation.

Marder, E. and Calabrese, R. L. (1996). "Principles of rhythmic motor pattern generation." Physiological Reviews **76**(3): 687-717.

McCrea, D. A. and Rybak, I. A. (2008). "Organization of mammalian locomotor rhythm and pattern generation." Brain Research Reviews **57**(1): 134-146.

Migliore, M., Hines, M. L. and Shepherd, G. M. (2005). "The role of distal dendritic gap junctions in synchronization of mitral cell axonal output." J Comput Neurosci **18**(2): 151-161.

Miller, J. P. and Selverston, A. I. (1982). "Mechanisms underlying pattern generation in lobster stomatogastric ganglion as determined by selective inactivation of identified neurons .2. Oscillatory properties of pyloric neurons." Journal of Neurophysiology **48**(6): 1378-1391.

Mirollo, R. E. and Strogatz, S. H. (1990). "Synchronization of pulse-coupled biological oscillators." Siam Journal on Applied Mathematics **50**(6): 1645-1662.

Moore, H. and Grace, A. A. (2002). "A role for electrotonic coupling in the striatum in the expression of dopamine receptor-mediated stereotypies." Neuropsychopharmacology **27**(6): 980-992.

Nargeot, R., Baxter, D. A. and Byrne, J. H. (1997). "Contingent-dependent enhancement of rhythmic motor patterns: An in vitro analog of operant conditioning." Journal of Neuroscience **17**(21): 8093-8105.

Nargeot, R., Baxter, D. A., Patterson, G. W. and Byrne, J. H. (1999). "Dopaminergic synapses mediate neuronal changes in an analogue of operant conditioning." Journal of Neurophysiology **81**(4): 1983-1987.

Nargeot, R., Cornet, C. and Simmers, J. (2008). Dopaminergic modulation of oscillatory membrane properties of buccal motor-pattern initiating neurons and their electrical coupling in *aplysia*. Forum of European Neuroscience, Geneva, Switzerland.

Nargeot, R., Le Bon-Jego, M. and Simmers, J. (2009). "Cellular and network mechanisms of operant learning-induced compulsive behavior in *aplysia*." Current Biology **19**: 975-984.

Nargeot, R., Petrissans, C. and Simmers, J. (2007). "Behavioral and in vitro correlates of compulsive-like food seeking induced by operant conditioning in aplysia." Journal of Neuroscience **27**(30): 8059-8070.

Netoff, T., Banks, M., Dorval, A., Acker, C., Haas, J., Kopell, N. and White, J. (2005). "Synchronization in hybrid neuronal networks of the hippocampal formation." J Neurophysiol. **93**(3): 1197-1208. Epub 2004 Nov 1193.

Netoff, T. I., Acker, C. D., Bettencourt, J. C. and White, J. A. (2005). "Beyond two-cell networks: Experimental measurement of neuronal responses to multiple synaptic inputs." Journal of Computational Neuroscience **18**(3): 287-295.

Oh, M. and Matveev, V. (2008). "Loss of synchrony in an inhibitory network of type-i oscillators." BMC Neuroscience **9**(Suppl 1): P149.

Oh, M. and Matveev, V. (2009). "Loss of phase-locking in non-weakly coupled inhibitory networks of type-i model neurons." Journal of Computational Neuroscience **26**(2): 303-320.

Olami, Z., Feder, H. J. S. and Christensen, K. (1992). "Self-organized criticality in a continuous, nonconservative cellular automaton modeling earthquakes." Physical Review Letters **68**(8): 1244-1247.

Oprisan, S. A. and Canavier, C. C. (2001). "Stability analysis of rings of pulse-coupled oscillators: The effect of phase resetting in the second cycle after the pulse is important at synchrony and for long pulses." Differential Equations and Dynamical Systems 9: 242-259.

Oprisan, S. A. and Canavier, C. C. (2005). "Stability criterion for a two-neuron reciprocally coupled network based on the phase and burst resetting curves." Neurocomputing 65: 733-739.

Oprisan, S. A., Prinz, A. A. and Canavier, C. C. (2004). "Phase resetting and phase locking in hybrid circuits of one model and one biological neuron." Biophysical Journal 87(4): 2283-2298.

Panchin, Y. V., Arshavsky, Y. I., Selverston, A. and Cleland, T. A. (1993). "Lobster stomatogastric neurons in primary culture .1. Basic characteristics." Journal of Neurophysiology 69(6): 1976-1992.

Perez Velazquez, J. L. and Carlen, P. L. (2000). "Gap junctions, synchrony and seizures." Trends Neurosci 23(2): 68-74.

Perez Velazquez, J. L., Carlen, P. L. and Skinner, F. K. (2001). "Artificial electrotonic coupling affects neuronal firing patterns depending upon cellular characteristics." Neuroscience 103(3): 841-849.

Phoka, E., Cuntz, H., Roth, A. and Hausser, M. (2008). Phase response curves in the presence of noise: A study of purkinje cell oscillatory dynamics. Cosyne Meeting, Salt Lake City.

Preyer, A. J. and Butera, R. J. (2005). "Neuronal oscillators in aplysia californica that demonstrate weak coupling in vitro." Physical Review Letters 95(13): 138103.

Preyer, A. J. and Butera, R. J. (2007). "The effect of residual electrode resistance and sampling delay on transient instability in the dynamic clamp system." 2007 Annual International Conference of the Ieee Engineering in Medicine and Biology Society, Vols 1-16: 430-433.

Prinz, A. A., Abbott, L. F. and Marder, E. (2004). "The dynamic clamp comes of age." Trends in Neurosciences 27(4): 218-224.

Prinz, A. A., Billimoria, C. P. and Marder, E. (2003). "Alternative to hand-tuning conductance-based models: Construction and analysis of databases of model neurons." Journal of Neurophysiology 90(6): 3998-4015.

Prinz, A. A., Thirumalai, V. and Marder, E. (2003). "The functional consequences of changes in the strength and duration of synaptic inputs to oscillatory neurons." Journal of Neuroscience 23(3): 943-954.

Reyes, A. D. and Fetz, E. E. (1993). "Two modes of interspike interval shortening by brief transient depolarizations in cat neocortical neurons." J Neurophysiol 69(5): 1661-1672.

Robertson, R. M. and Moulins, M. (1981). "Firing between two spike thresholds: Implications for oscillating lobster interneurons." Science 214(4523): 941-943.

Rodriguez, E., George, N., Lachaux, J. P., Martinerie, J., Renault, B. and Varela, F. J. (1999). "Perception's shadow: Long-distance synchronization of human brain activity." Nature 397(6718): 430-433.

Selverston, A. I. and Moulins, M. (1987). The crustacean stomatogastric system. Berlin, Springer-Verlag.

Selverston, A. I., Rabinovich, M. I., Abarbanel, H. D. I., Elson, R., Szucs, A., Pinto, R. D., Huerta, R. and Varona, P. (2000). "Reliable circuits from irregular neurons: A dynamical approach to understanding central pattern generators." Journal of Physiology-Paris **94**(5-6): 357-374.

Sharp, A. A., O'Neil, M. B., Abbott, L. F. and Marder, E. (1993). "The dynamic clamp - artificial conductances in biological neurons." Trends in Neurosciences **16**(10): 389-394.

Sharp, A. A., O'Neil, M. B., Abbott, L. F. and Marder, E. (1993). "Dynamic clamp - computer-generated conductances in real neurons." Journal of Neurophysiology **69**(3): 992-995.

Sherman, A. and Rinzel, J. (1992). "Rhythmogenic effects of weak electrotonic coupling in neuronal models." Proc Natl Acad Sci U S A **89**(6): 2471-2474.

Sieling, F. H. (2009). 4 channel dynamic clamp implementation using spike2 and 1401plus. CED eNews: The eNewsletter from Cambridge Electronic Design.

Sieling, F. H., Canavier, C. C. and Prinz, A. A. (2009). "Predictions of phase-locking in excitatory hybrid networks: Excitation does not promote phase-locking in pattern-generating networks as reliably as inhibition." J Neurophysiol **102**(1): 69-84.

Sieling, F. H., Canavier, C. C. and Prinz, A. A. (2010). "Inclusion of noise in iterated firing time maps based on the phase response curve." Physical Review E **81**(6): 061923.

Skinner, B. F. (1938). The behavior of organisms: An experimental analysis. New York, Appleton-Century-Crofts.

Soto-Trevino, C., Rabbah, P., Marder, E. and Nadim, F. (2005). "Computational model of electrically coupled, intrinsically distinct pacemaker neurons." J Neurophysiol **94**(1): 590-604.

Strogatz, S. H. (2003). Sync: The emerging science of spontaneous order, Hyperion.

Susswein, A. J., Hurwitz, I., Thorne, R., Byrne, J. H. and Baxter, D. A. (2002). "Mechanisms underlying fictive feeding in aplysia: Coupling between a large neuron with plateau potentials activity and a spiking neuron." J Neurophysiol **87**(5): 2307-2323.

Susswein, A. J., Schwarz, M. and Feldman, E. (1986). "Learned changes of feeding behavior in aplysia in response to edible and inedible foods." J Neurosci **6**(5): 1513-1527.

Talathi, S. S., Hwang, D.-U., Miliotis, A., Carney, P. R. and Ditto, W. L. (2009). "Predicting synchrony in heterogeneous pulse coupled oscillators." Physical Review E **80**(2): 021908.

Tazaki, K. and Cooke, I. M. (1990). "Characterization of ca current underlying burst formation in lobster cardiac ganglion motorneurons." J Neurophysiol **63**(2): 370-384.

Thorndike, E. L. (1911). Animal intelligence: Experimental studies. New York, Macmillan.

Thorndike, E. L. (1933). "A proof of the law of effect." Science **77**(1989): 173-175.

Timme, M., Wolf, F. and Geisel, T. (2002). "Coexistence of regular and irregular dynamics in complex networks of pulse-coupled oscillators." Physical Review Letters **89**(25).

Tsubo, Y., Takada, M., Reyes, A. D. and Fukai, T. (2007). "Layer and frequency dependencies of phase response properties of pyramidal neurons in rat motor cortex." Eur J Neurosci **25**(11): 3429-3441.

Turrigiano, G., LeMasson, G. and Marder, E. (1995). "Selective regulation of current densities underlies spontaneous changes in the activity of cultured neurons." Journal of Neuroscience **15**(5): 3640-3652.

Velazquez, J. L. P., Galan, R. F., Dominguez, L. G., Leshchenko, Y., Lo, S., Belkas, J. and Erra, R. G. (2007). "Phase response curves in the characterization of epileptiform activity." Physical Review E **76**(6).

Winfree, A. T. (2001). The geometry of biological time. New York, Springer.

Woodman, M. M. and Canavier, C. C. (2008). A mechanism for synchronization in the presence of delays in which strong coupling compensates for deviations from symmetry. Society for Neuroscience, Washington D.C.

Woodman, M. M. and Canavier, C. C. (2009). Phase locking of pulse-coupled oscillators with delays is determined by the phase response curve. COSYNE Meeting. Salt Lake City, Utah.

Young, M. P., Tanaka, K. and Yamane, S. (1992). "On oscillating neuronal responses in the visual cortex of the monkey." J Neurophysiol **67**(6): 1464-1474.

Zhao, S., Golowasch, J. and Nadim, F. (2010). "Pacemaker neuron and network oscillations depend on a neuromodulator-regulated linear current." Front Behav Neurosci **4**: 21.

Ziburkus, J., Cressman, J. R., Barreto, E. and Schiff, S. J. (2006). "Interneuron and pyramidal cell interplay during in vitro seizure-like events." Journal of Neurophysiology **95**(6): 3948-3954.